University of Central Lancashire UCLan

Central Lancashire Online Knowledge (CLoK)

Title	Plasmonic nanoparticle-based surface-enhanced Raman spectroscopy-guided photothermal therapy: emerging cancer theranostics
Type	Article
URL	https://clok.uclan.ac.uk/46770/
DOI	https://doi.org/10.2217/nnm-2023-0010
Date	2023
Citation	Das, Anindita, Tsai, Hsieh-Chih, Sen, Tapas and Moirangthem, Rakesh S (2023) Plasmonic nanoparticle-based surface-enhanced Raman spectroscopy-guided photothermal therapy: emerging cancer theranostics. Nanomedicine. ISSN 1743-5889
Creators	Das, Anindita, Tsai, Hsieh-Chih, Sen, Tapas and Moirangthem, Rakesh S

It is advisable to refer to the publisher's version if you intend to cite from the work. https://doi.org/10.2217/nnm-2023-0010

For information about Research at UCLan please go to http://www.uclan.ac.uk/research/

All outputs in CLoK are protected by Intellectual Property Rights law, including Copyright law. Copyright, IPR and Moral Rights for the works on this site are retained by the individual authors and/or other copyright owners. Terms and conditions for use of this material are defined in the http://clok.uclan.ac.uk/policies/

Review

For reprint orders, please contact: reprints@futuremedicine.com

Nanomedicine

Plasmonic nanoparticle-based surface-enhanced Raman spectroscopy-guided photothermal therapy: emerging cancer theranostics

Anindita Das[1], Hsieh-Chih Tsai[3,4,5], Tapas Sen*[,6] & Rakesh S Moirangthem**[,1,2]

[1]Department of Physics, Nanophotonics Lab, Indian Institute of Technology (Indian School of Mines), Dhanbad, Jharkhand, 826004, India

[2]Department of Physics, Manipur University, Canchipur, Imphal, Manipur, 795003, India

[3]Graduate Institute of Applied Science & Technology, National Taiwan University of Science & Technology, Taipei, 106, Taiwan

[4]Advanced Membrane Materials Center, National Taiwan University of Science & Technology, Taipei, 106, Taiwan

[5]R&D Center for Membrane Technology, Chung Yuan Christian University, Chungli, Tao-Yuan, 320, Taiwan

[6]Nano-biomaterials Research Group, School of Natural Sciences, Faculty of Science & Technology, University of Central Lancashire, Preston, PR1 2HE, United Kingdom

*Author for correspondence: tsen@uclan.ac.uk

**Author for correspondence: rakesh@manipuruniv.ac.in

Optical imaging modalities have emerged as a keystone in oncological research, capable of providing molecular and cellular information on cancer with the advantage of being minimally invasive toward healthy tissues. Photothermal therapy (PTT) has shown great potential, with the exceptional advantages of high specificity and noninvasiveness. Combining surface-enhanced Raman spectroscopy (SERS)-based optical imaging with PTT has shown tremendous potential in cancer theranostics (therapeutics + diagnosis). This comprehensive review article provides up-to-date information by exploring recent works focused mainly on the development of plasmonic nanoparticles for medical applications using SERS-guided PTT, including the fundamental principles behind SERS and the plasmon heating effect for PTT.

Graphical abstract:

Future Medicine

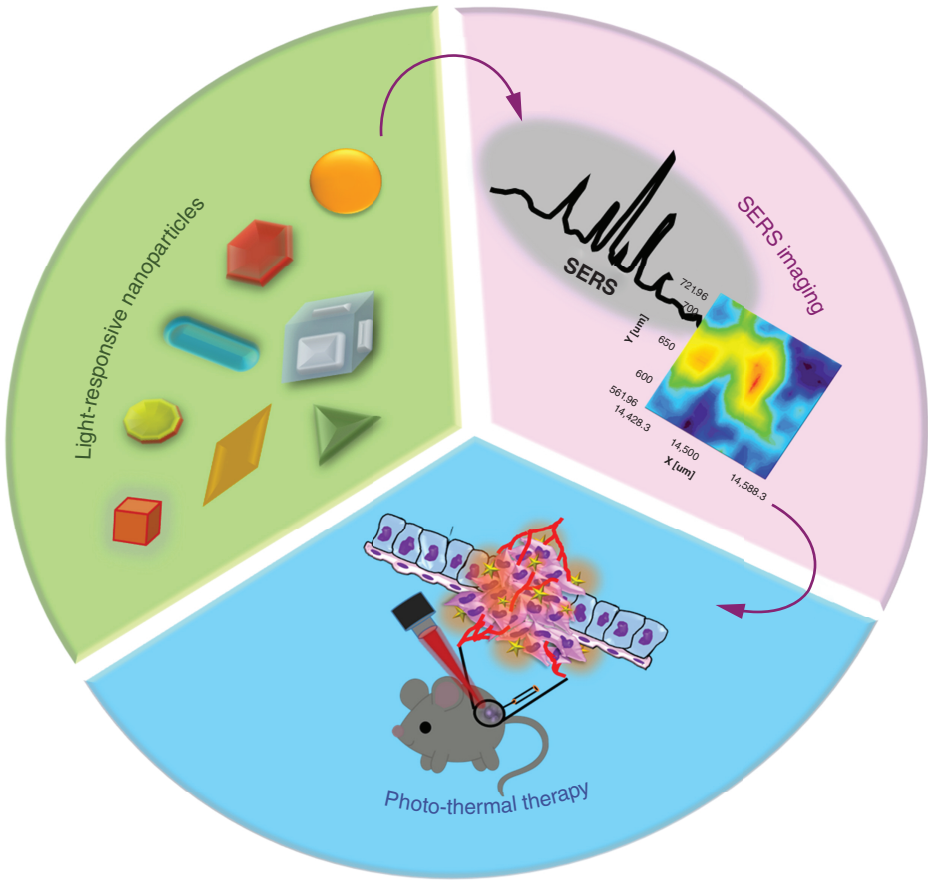

First draft submitted: 16 January 2023; Accepted for publication: 20 March 2023; Published online: TBC

Keywords: cancer theranostics • photothermal therapy • plasmonic nanoparticles • surface-enhanced Raman spectroscopy • surface functionalization • toxicity

Today, cancer treatment that is minimally invasive is one of the biggest challenges for clinicians and the scientific community. Diagnosing cancer at an early stage, identifying metastatic lymph nodes, providing noninvasive or less invasive therapies with high specificity and reducing treatment costs are essential needs in oncological medicine. Recently, nanotechnology-based theranostic strategies have shown tremendous potential in various clinical applications [1,2]. In this context, plasmonic nanoparticles (NPs) have received enormous research interest in the last few decades due to their excellent physicochemical properties, dealing with light confinement and manipulation at the nanoscale level and acting as a bridge between various physical, chemical and biological studies. Among several potential applications, plasmonic nanomaterials have had a tremendous impact on bioscience applications such as bio-sensing, bio-imaging and cancer theranostics [3–6]. The surface plasmon resonance effect in noble metals is due to the collective oscillations of free electrons in resonance with incident photon frequencies and resulting in an intense electromagnetic (EM) field confinement at the metal surface. When the noble metals are in nm dimension and the size is smaller than or comparable to the wavelength of incident radiation, then surface plasmon waves are confined within the domain known as the localized surface plasmon resonance (LSPR) effect [7,8]. LSPR is a widespread phenomenon having two important aspects: a macroscopic local electric field around the metallic nanostructures, which is maximum at the surface and decays exponentially by increasing the distance from the metallic surface, and the optical extinction coefficient of the NPs is maximum at the resonant frequency [9]. Further, the plasmonic properties of NPs strongly depend on the particles' geometrical parameters, the refractive index of the surrounding medium, the composition and so on. Unique optical tunability, easy functionalization with various biomolecules, good dispersibility in an aqueous medium and excellent biocompatibility make plasmonic NPs a suitable therapeutic along with optically stable multimodal imaging agents [10]. Metal NPs such as gold (Au) and silver (Ag) have already shown promising plasmonic properties, whereas hybrid NPs such as metal oxides,

chalcogenides, dielectrics and polymer nanocomposites with noble metals recently receiving attention due to their composition, which is unattainable by single-component nanostructures [11–13]. Therefore, plasmonic NPs can behave as a nanosource of localized heat and light due to the generation of hot carriers and an enhanced local EM field upon laser irradiation. However, tuning their heating efficiency requires careful engineering from an application point of view [3].

Photothermal therapy (PTT) is a recent technique in which photoactive NPs generate localized heat upon laser irradiation for hypothermic ablation of cancer cells. PTT provides some unique advantages over conventional cancer therapies, such as precise spatial-temporal selectivity, high specificity, minimal invasiveness and cost–effectiveness [1,14,15]. Dating back to the 19th century, a partial tumor regression was first observed in a patient having a fever. Since then, a lot of effort has been expended to understand the mechanism of temperature-induced cell death. Modern thermal treatments have a huge potential to serve as an alternative to radiation and chemotherapy. Generally, carcinogenic tumor sites are involved with disordered vasculature and deficient blood supply, making them more prone to heat than healthy tissues. Therefore, well-designed plasmonic NPs can generate heat to the location of interest (localized heat) without affecting the healthy tissues under laser irradiation [16–19].

Further, PTT can be guided by multimodal imaging techniques using plasmonic NPs to provide better insight into thermal ablation during therapy. The optical imaging techniques have several advantages, such as good spatial resolution, use of the optical properties of the bio-tissue to generate contrast images and real-time bedside monitoring. Confocal fluorescence microscopy is an excellent optical imaging tool that provides 3D images over a typical spatial resolution of volume $(500 \times 500 \times 1000)\ nm^3$ [20–22]. This resolution permits real-time monitoring of fluorescently labeled probe molecules, including antibodies, proteins, various drug molecules and their metabolic activities. However, the size of fluorescent labels, usually an organic dye molecule, is often large compared with a small molecule; rapid photobleaching and low quantum yield values limit the analysis of molecular details at the intracellular level. Similarly, the optical coherence tomography technique does not provide chemical contrast. However, vibrational spectroscopic techniques, such as infrared (IR) and Raman imaging, generate contrast based on the specimen's chemical composition. Furthermore, IR imaging is not a suitable option for study related to biomolecules and cells in an aqueous medium due to the strong IR absorbance of water. In that case, Raman spectroscopy delivers better results, as water is a weak Raman scatterer [23,24]. Due to this property under physiological conditions, Raman imaging has attracted major research interest, as tissue monitoring is possible without contrast agents, it provides good spatial resolution, the Raman signal intensity can be enhanced further using the surface-enhanced Raman spectroscopy (SERS) technique to detect probe molecules and the contrast-enhancing probes are able to cross the cell membrane and identify DNA sequences, cancer biomarkers, enzymes, nucleic acids and several intracellular processes. In addition, the SERS technique not only preserves the vital features of Raman scattering but also provides highly sensitive and efficient signal detection even up to the single-molecule level in the bio-imaging process [25–28].

Regarding these aspects of research, it has been confirmed that the combination of SERS and PTT techniques provides numerous advantages in cancer theranostics. Real-time monitoring of temperature-induced intracellular changes by combined SERS–PTT techniques using plasmonic NPs for selectively killing carcinoma cells without affecting healthy cells upon laser irradiation is possible [29]. Despite many technical and biological challenges, plasmonic PTT combined with Raman imaging has proven to possess great potential in multimodal oncological strategies. Several multifunctional plasmonic NPs have been developed, and their use as SERS–PTT dual-functioning probes is currently a hot research topic with future potential.

Several review articles have summarized the importance of plasmonic NPs separately as SERS imaging or PTT agents separately without discussing much as a combined techniques (SERS +PTT) [1,30–33]. Moreover, reviews with special focus on plasmonic NP-based SERS-guided PTT are rare.

This review provides a general overview by covering the latest development of SERS–PTT as combined techniques in cancer theranostics, the advantages, the current challenges and the future direction.

Concept of SERS & PT effect in plasmonic NPs

Principles of SERS

SERS comes under surface spectroscopy techniques, where the analyte molecules must be on or at proximity to the metallic NP. Amplification of the Raman signal is possible in two ways: EM enhancement due to the plasmon resonances in metallic nanostructures and chemical enhancement (CE) as the Raman polarizability of the analyte molecule is increased due to absorption on a metallic surface [34,35]. The SERS enhancement factor (EF) due to

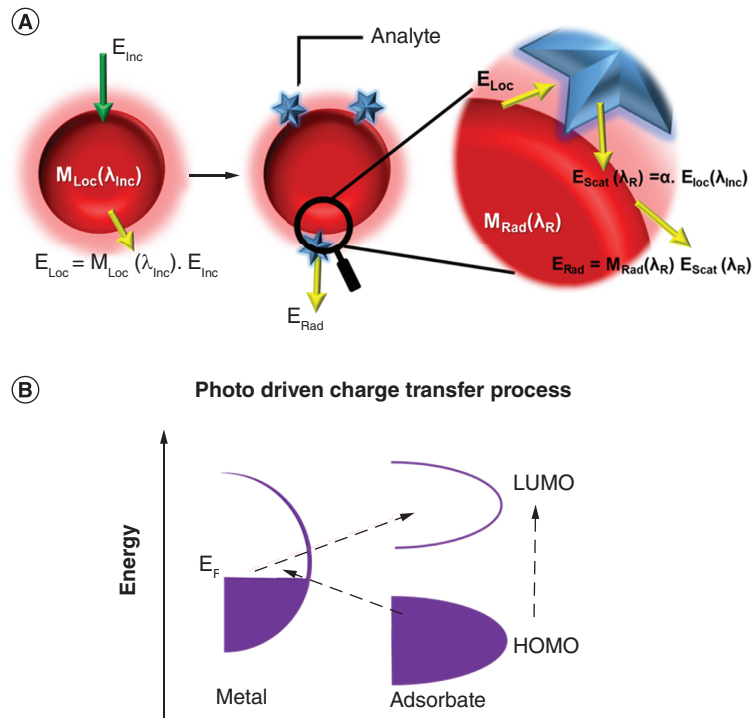

Figure 1. Mechanisims involved in SERS enhancement. (A) Schematic of electromagnetic enhancement in the surface-enhanced Raman spectroscopy process: nanoparticle (NP) excitation due to incident radiation (E_{Inc}) leads to local field (E_{Loc}) enhancement, which further interacts with the analyte molecule at the vicinity of the NP. The molecule is excited by the local field and scatters and radiates an enhanced scattered field at Raman wavelength (λ_R), and in the reradiation process, the scattered field interacts with the NP's local field and is enhanced further. **(B)** Illustration of charge-transfer resonance enhancement.
HOMO: Highest occupied molecular orbital; LUMO: Lowest unoccupied molecular orbital.
Data from [36,37].

EM enhancement ($EF_{EM} \approx 10^4$–10^{10}) is considered dominant over CE ($EF_{CE} \approx 10^1$–10^2) which is much smaller compaired to EM. To clarify, this review discusses these two effects in detail in the following sections.

EM enhancement

EM enhancement is believed to be the main contribution to the overall EF. This approach is applicable to all analytes, and it is an instantaneous, two-step process. The first one is the enhanced incident field (E_{Loc}) due to the interaction between the incident field (E_{Inc}) and the metallic nanostructure, as shown in Figure 1A [36].

This microscopic local electric field is a function of incident wavelength (λ_{Inc}) and induces a Raman dipole (pR) with a magnitude of $\frac{|E_{Loc}(\lambda_{Inc})|}{|E_{Inc}|}$, which radiates energy in free space in the order of $|pR|^2$. Therefore, the microscopic local electric field can be expressed as

$$E_{Loc} = M_{Loc}(\lambda_{Inc}) \cdot E_{Inc} \qquad \text{(Equation 1)}$$

$M_{Loc}(\lambda_{Inc})$ is known as the local field intensity EF, and it depends on the magnitude of Raman dipole – that is, $M_{Loc}(\lambda_{Inc}) = |E_{Loc}(\lambda_{Inc})|^2/|E_{Inc}|^2$.

Simultaneously, the analyte molecule interacts with the local electric field and scatters the Raman signal in all possible directions. The scattered electric field is a function of Raman wavelength (λ_R), which can be described as

$$E_{Scat}(\lambda_R) = \alpha \cdot |E_{Loc}(\lambda_{Inc}) \qquad \text{(Equation 2)}$$

where α is the molecular polarizability. Here, λ_R is shifted from λ_{Inc}, and the scattered field is enhanced by the induced local field of the NP. Again, in the second phase, reradiation occurs due to the interaction between the scattered electric field and the NP's local field. Therefore, the reradiated enhanced electric field can be expressed as

$$E_{Rad} = M_{Rad}(\lambda_R) \cdot E_{Scat}(\lambda_R) = \alpha \cdot M_{Loc}(\lambda_{Inc}) \cdot M_{Rad}(\lambda_R) \cdot E_{Inc} \qquad \text{(Equation 3)}$$

where $M_{Rad}(\lambda_R)$ is the directional radiation EF in the direction of the SERS signal detector. The directional factor matters due to the possibility of signal quenching if the enhanced signal deflects away from the detector. Finally, by considering two main mechanisms of excitation and re-emission, the intensity of the Raman EF (I_{SERS}) can be written as

$$I_{SERS} = M_{Loc}(\lambda_{Inc}) \cdot M_{Rad}(\lambda_R) \cdot I_{Inc} = (SMIEF) \cdot I_{Inc} \qquad \text{(Equation 4)}$$

The factor $M_{Loc}^2(\lambda_{Inc}) \cdot M_{Rad}^2(\lambda_R)$ represents the single-molecule intensity EF (SMIEF), and SMIEF is a function of λ_{Inc} and λ_R. Further, if both the wavelengths are close to each other, then SMIEF can be represented as

$$SMEF(\lambda_R) = M_{Loc}(\lambda_R) = \frac{|E_{Loc}(\lambda_{Inc})|^4}{|E_{Inc}|^4} \quad \text{(Equation 5)}$$

From this mathematical expression, it can be understood that the SERS enhancement is almost at the 4th power of the local electric field enhancement near the vicinity of the metal NP and the basis for the well-known $|E|^4$-approximation theory [38,39]. However, the exact influence on total enhancement has not been confirmed yet [40].

Therefore, by considering the EM theory, the above explanation seems highly relevant to explain the mechanism of EM-SERS enhancement. Still, some underlying physics such as the polarization effect demands further research [41]. Nevertheless, analysis of the SERS EF by considering the microscopic local electric field provides a much simpler understanding of the study. Therefore, if the probe molecule gets adsorbed on the metallic NP surface, the strong localized plasmon-induced electric field improves the molecule's SERS signal intensity. The plasmon-assisted intense local electric field (hot spots) across metal NPs are central to intense Raman scattering.

CE effect

CE results from the increase in molecular polarizability of the analyte due to the charge transfer (CT) between the metal and the analyte molecule [42]. New transitions occur as the electronic states of the analyte molecule interact with the metal. In such interactions, the difference between the Fermi level (E_F) of the metal and the highest occupied molecular orbital or lowest unoccupied molecular orbital energies have resonance with the incident laser radiation, as shown in Figure 1B. Such a photo-driven charge-transfer mechanism can be understood through electrochemical cell experiments [38,43]. Molecular simulation methods such as density functional theory and molecular dynamics are also powerful tools to identify molecular interactions with the metallic nanostructures [44]. Unlike EM-SERS enhancement, CE is probe-dependent; bonding is necessary between the metal and probe molecule. Further, EM enhancement theory cannot explain certain observations, such as the difference between the SERS spectrum and the normal Raman spectrum of the same molecules and the change in enhancement factors when different analyte molecules are being tested on the same SERS substrate with the same experimental conditions. Such observations can be explained using CE concepts.

Principles of the photothermal effect

Noble metals have emerged as efficient photothermal transducers, and the LSPR effect associated with plasmonic NPs induces an additional heating effect. To explore the nanotechnology-based hyperthermia treatments, the basic processes responsible for light-to-heat conversion need to be understood and are discussed in this section.

Hot carrier generation & heating up the surroundings

On resonant excitation of plasmonic NPs, the plasmons are relaxed within ~1–100 fs. The relaxation proceeds radiatively by photon re-emission (scattering) or nonradiatively by Landau damping (absorption). The decay of excited plasmons to hot electron-hole pairs is a pure quantum mechanical process. A nonthermal hot electron-holes distribution above and below the Fermi energy level due to photoexcitation is shown in Figure 2A [45]. Further, these hot carriers adiabatically lose energy by transferring the power to the lattice via electron–electron scattering to obey a Fermi–Dirac-like distribution on a timescale of 100 fs to 1 ps with a large effective electron temperature (T_{el}), as illustrated in Figure 2B & C. These complex processes can be explained by the two-temperature model, which is a coupled two-step process of absorption of incident photon energy by electrons, followed by heating of lattice due to electron–phonon collisions [46]. Thus, the electron energy is transferred to the lattice via electron–phonon coupling factor to reach the equilibrium between lattice temperature (T_l) and electron temperature (T_{el}) over a timescale of several ps. Finally, depending on the nature of the materials, particle size, and thermal conductivity of the surrounding media, the energy is dissipated across the nanodomain by phonon–phonon interaction and radiates to the NP's surrounding in the form of heat within an ~100 ps to 10 ns timescale [46,47].

The lattice transfers energy to NPs surroundings in the form of heat within a nanosecond timescale. The temperature distribution by heat transfer model can be described by considering the usual heat transfer (Equation 6) of a uniformly heated spherical NP in an infinite homogeneous medium [48].

$$\rho(r)c(r)\frac{\partial T(r,t)}{\partial t} = K\Delta T(r,t) + Q(r,t) \quad \text{(Equation 6)}$$

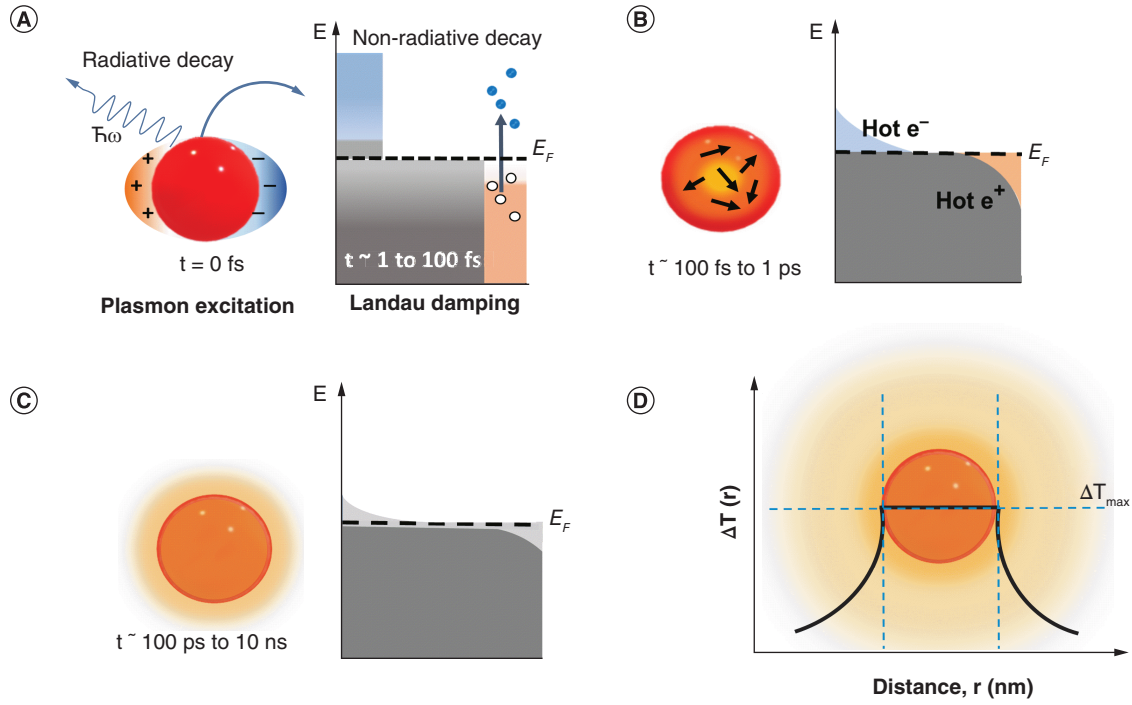

Figure 2. Plasmon induced local heat in nanoparticle. Stepwise time evolution of plasmon-induced electronic excitation and relaxation of a metallic nanoparticle (NP) with electronic energy distribution diagram **(A–C)**, where the Y-axis represents the energy **(E)** and the Fermi energy is labeled E_F. **(A)** Radiative and nonradiative decay of excited localized surface plasmons in the NP, generating hot carriers. In the nonradiative decay process, the photo-excited electrons jump from filled to unfilled states, generating a nonthermal electron distribution. The grey shadings are the filled electronic states, whereas the blue and white dots represent the hot electrons and holes. **(B)** Redistribution of the energy via electron–electron scattering and thermalization through a higher electron temperature. **(C)** The hot electron distribution cools over time due to carrier relaxation through lattice heating. **(D)** Schematic representation of a photo-excited NP with the temperature distribution plot across the NP as a function of distance. Data from [46].

where $T(r,t)$ is the local temperature, which is a function of position coordinate (r) and time (t); $\rho(r)$ is the mass density; $c(r)$ is specific heat; K is the thermal conductivity; and $Q(r,t)$ is the source term, which comes from heat generation inside the NP due to incident light. It can be expressed as $Q(r, t) = \sigma_{abs} I$, where σ_{abs} is the NP's absorption cross section and I is the incident light intensity. Further, for the case of nonmagnetic lossy media, the source term can be expressed as a function of electric field $E(r,t)$ and the imaginary part of the dielectric function $\epsilon(r, \omega)$:

$$Q(r, t) = \frac{\omega}{2\pi} Im\,[\varepsilon(r, \omega)]\,|E(r, t)|^2 \qquad \text{(Equation 7)}$$

where ω is the incident light frequency and ϵ is the electric permittivity of the NP. The source term also represents the time-averaged energy density for the absorptive power dissipation of the NP [49,50].

In the steady-state and continuous laser pulse illumination regimes, the local temperature distribution around a single NP system is given as

$$\Delta T(r) = \frac{V_{NP} Q}{4\pi K_0 r} \qquad \text{(Equation 8)}$$

where V_{NP} is the NP volume, K_0 is the thermal conductivity of the surrounding medium and r is the distance from the center of the NP. Further, the maximum temperature gradient ΔT_{max} occurs at the NP surface, as illustrated in Figure 2D. The time-dependent heat equation provides a relationship between temperature gradient (ΔT) and NP size (R_{NP}) as $\Delta T_{\max} \propto R_{NP}^2$, indicating that the total heat generation rate depends on the physical properties (i.e., the size of the materials) [51].

Influencing factors in designing SERS-guided PTT nanoprobes

During PTT, human tissues exhibit a high extinction coefficient in the visible range, and the irradiated light energy is absorbed by both healthy and cancerous tumor tissues. Consequently, it creates unwanted damage to adjacent healthy tissues and limits its therapeutic efficacy. However, incorporating photo-absorbers such as NPs into tumors allows the reduction of abnormal tissue heating in the surrounding healthy tissues with the maximum conversion of photon energy to heat [52]. The combination of SERS and PTT techniques has been advantageous in real-time imaging-guided cancer therapies. Therefore, while designing and fabricating an efficient nanoprobe, necessary influential physicochemical factors need to be considered, so that there is no compromise on the SERS signal enhancement and thermal therapy efficiency. Research efforts have mainly focused on identifying the role of NP geometry, surface chemistry and biocompatibility of various plasmonic NPs for theranostics application [53].

Impact of shape, size & composition

Designing and incorporating plasmonic nanoprobes is challenging due to their complex synthesis route and their optimum performance in *in vivo* and *in vitro* bio-environments. All classic active SERS plasmonic materials such as Ag, Au and copper (Cu) NPs and a combination of plasmonic with nonplasmonic materials as nanocomposites are known to be good thermal ablation agents [54,55]. Plasmonically engineered nanoprobes can be classified as basic nanostructures or complex nanocomposites (see Supplementary Figure 1). Further, precise control on the absorption spectra over the visible to near-infrared (NIR) range is possible by controlling the nanomaterial's composition, shape and size [56,57]. Light wavelength in the biological window makes tissues become partly transparent due to the reduction of their extinction coefficient, mainly affected by the optical absorption of water, hemoglobin and so on (see Figure 3A). Current studies mainly focus on the first biological window (NIR-I; 700–980 nm), whereas the second biological window (NIR-II; 1000–1400 nm) has been less investigated. Therefore, designing NPs with high photothermal transduction capacity and a wide absorption cross section for incident radiation from the NIR-I to NIR-II window provides deep tissue treatments and reduces the undesired heating of healthy tissues. It also makes PTT conceivable with low-power laser sources [58]. Using a specific laser wavelength under the so-called biological windows limits tissue self-heating and gives the maximum permissible exposure (MPE) to light [52].

Most of the plasmonic metal-based NPs used in clinical studies are spherical. In contrast to nanospheres, nanorods (NRs) exhibit dual plasmon modes typically from the UV-visible to IR spectral range, and the LSPR peak position can be tuned by varying their aspect ratio. Takahata *et al.* synthesized cetyltrimethylammonium bromide (CTAB)-coated ultrathin Au NRs of different aspect ratios; their LSPR band can be tuned up to the mid-IR region by tuning the aspect ratios (Figure 3B) [61]. Other anisotropic geometries (e.g., nanostars [size range: 100–200 nm]) are also popular, as their LSPR band can be modulated by simply manipulating their nanotip sharpness, branch numbers and length. (Figure 3C) illustrates synthesized Au nanostars (synthesized using optimized reactant ratios and temperatures) with different morphologies, sizes (45–100 nm) and corresponding LSPR peak absorbance values [62]. Upon increasing the size and extent of anisotropy a red shift in the resonance condition can be achieved. However, increasing the size limits their efficiency in *in vivo* application due to low blood circulation periods, which limits the delivery of NPs to tumor sites via leaky vasculature [64]. Further, using plasmonically engineered, bimetallic, metal–semiconductor and metal–polymer nanocomposites can also provide near to far IR LSPR absorbance. Bhattacharya *et al.* have reported that a bimetallic Au core with spherical Ag shell (both solid and hollow), Au core with cubical Ag shell (both solid and hollow) NPs and Au@Ag nanocubes (both solid and hollow) showed a wide range of NIR absorbance values (Figure 3D) [59].

The plasmonic properties of nanocomposite systems can be controlled by controlling the shapes and sizes, which provides different quantum confinements and surface properties near nanojunctions. The hybrid metal–semiconductor composites with a combination of the individual materials' properties can offer an entirely new class of photo-physical properties. Zhu *et al.* have adopted a modified self-limiting and self-assembly-based hydrothermal synthesis route for fabricating monodisperse dual plasmonic Au@$Cu_{2-X}S$ and Au@$Cu_{2-X}Se$ NPs. The hybrid NPs have two distinct LSPR bands covering visible to NIR regions (Figure 3E). The presence of a strong NIR band is due to the coupling effects of the plasmonic core and $Cu_{2-X}S$ shell layer [63]. The NIR bio-window (NIR-II: 1000–1350 nm) can provide MPE, and advanced nanoprobes with NIR-II LSPR absorbance can hold great promise. Recently, an interesting nanomaterial composed of an Au nanoframework (Au NF) with mesopores showed strong LSPR absorbance in the NIR-II bio-window, as shown in (Figure 3F) [60]. Such NPs would provide higher tissue penetration depth with efficient photothermal conversion in deep tumor therapy.

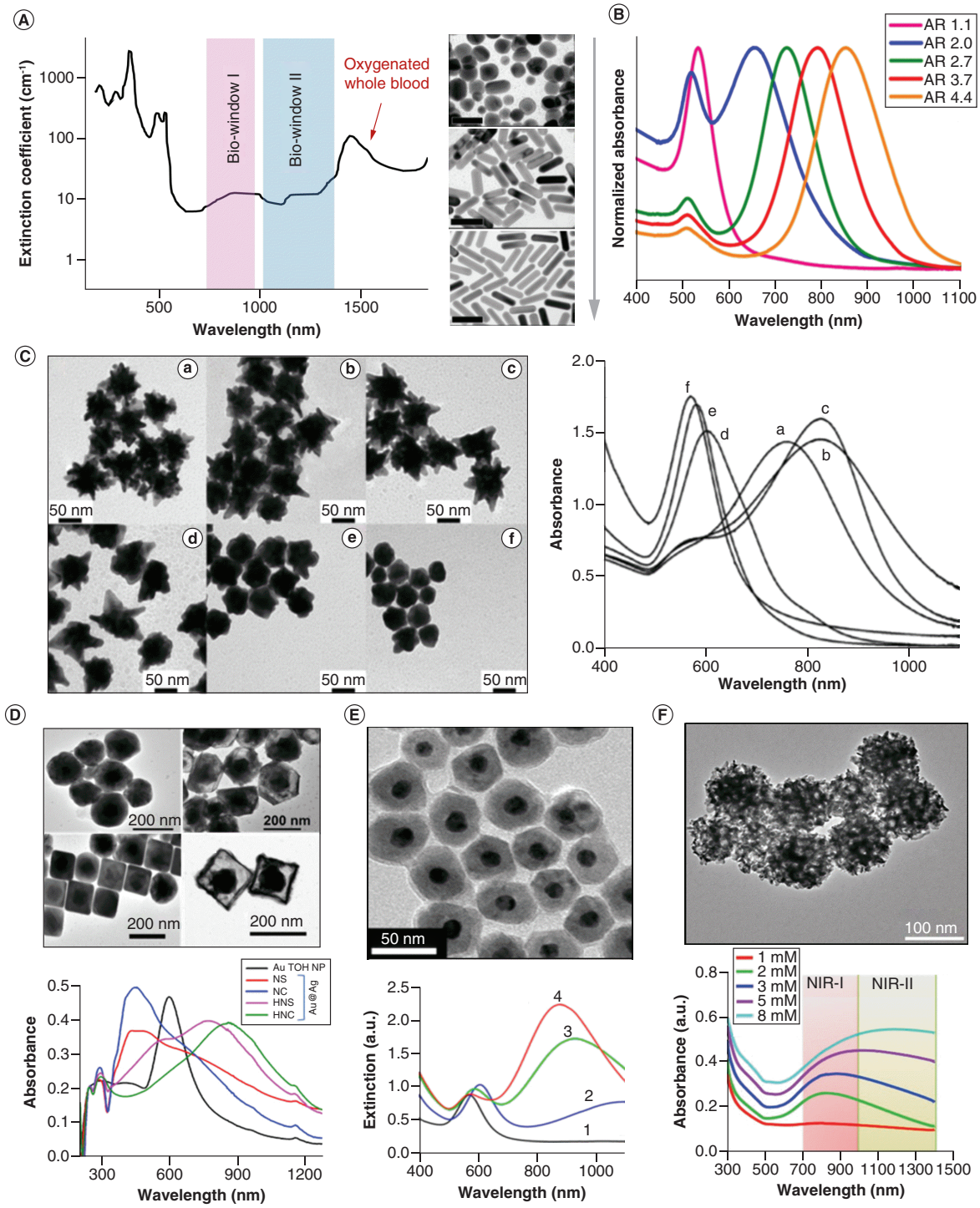

Figure 3. Shape, size & composition effect on LSPR absorption of nanostructures. (A) Extinction spectra of a representative biological tissue with first and second biological windows range. **(B)** Transmission electron microscopy (TEM) images of Au nanorods with different aspect ratios and their UV-visible spectra showing the tuning of localized surface plasmon resonance absorbance by tuning the aspect ratios. Copyright (2014), American Chemical Society. **(C)** Shifting of localized surface plasmon resonance peak position depending on change in nanostar tip sharpness. Copyright (2010), American Chemical Society. **(D)** TEM image of gold (Au) core and spherical silver (Ag) shell (both solid and hollow) and Au core and cubical Ag shell (both solid and hollow) nanoparticles (NPs) and their corresponding absorbance spectra. Reproduced with permission from [59]. **(E)** TEM image of monodispersed Au@$Cu_{2-x}S$ core-shell NPs and their extinction spectra with two distinct plasmon bands. Copyright (2017), American Chemical Society. **(F)** Fabricated porous Au nanoframeworks using liposomes as a template and their widespread absorbance up to second biological window region.
Reprinted with permission from [60]. Copyright (2020) John Wiley and Sons. Data from [58–63].

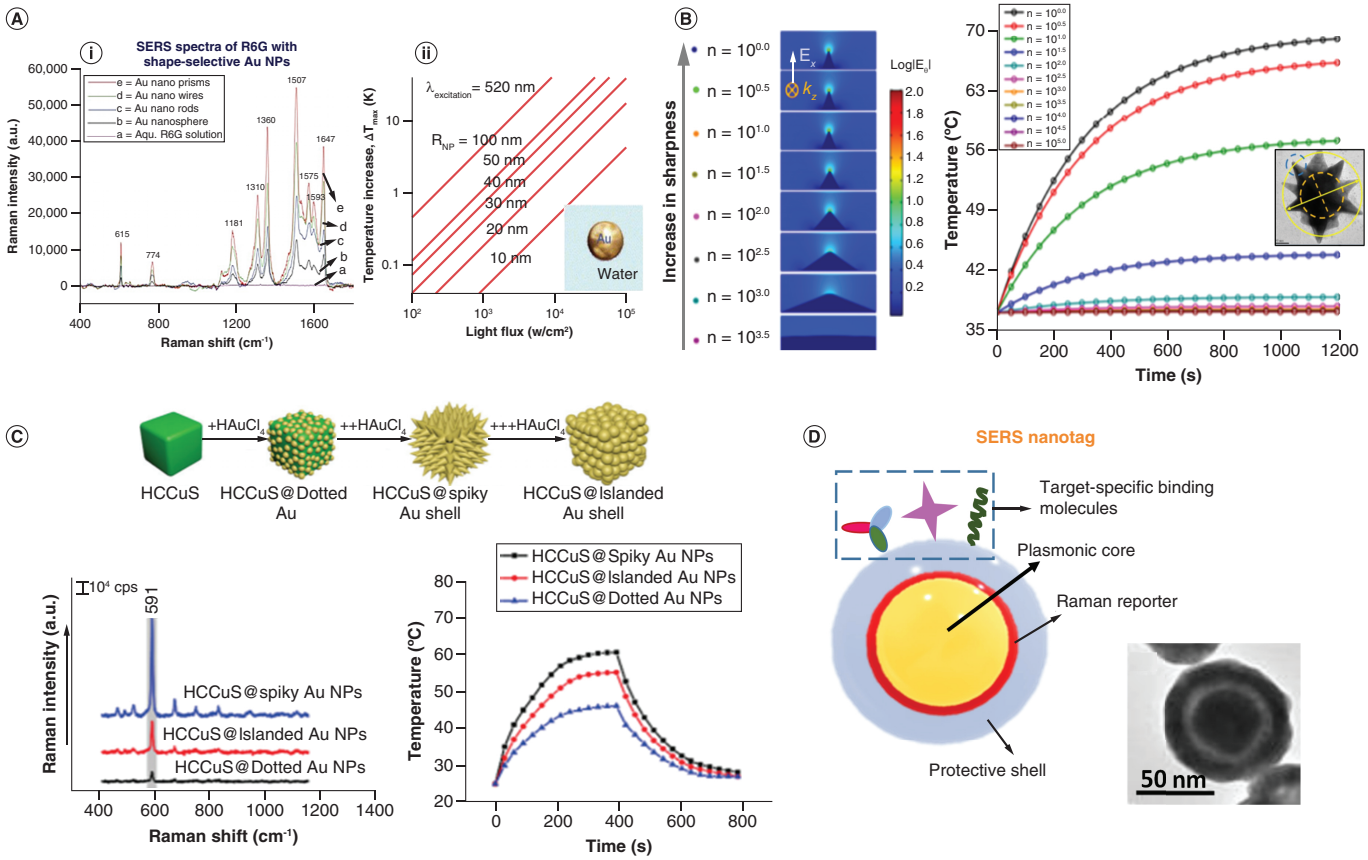

Figure 4. Plasmon induced local electric field enhancement and the photothermal conversion in nanostructures. (A) (I) Normal Raman and surface-enhanced Raman spectroscopy (SERS) spectra of Rd6G mixed with shape-selective gold (Au) nanoparticles (NPs) at a fixed concentration. Copyright (2012), Royal Society of Chemistry. **(II)** Photothermal properties based on NP shape. Copyright (2007) Elsevier. **(B)** Tuning of electric field intensity and photothermal therapy temperature depending on tip sharpness of nanostar with transmission electron microscopy image of synthesized Au nanostar. Copyright (2018), American Chemical Society. **(C)** Schematic of synthesis steps and comparisons of SERS and photothermal therapy efficiency of hollow cubic copper sulfide (CuS) NPs, HCCuS@ dotted Au, HCCuS@ spiky Au and HCCuS@ islanded Au NPs. Copyright (2018), Royal Society of Chemistry. **(D)** Schematic of SERS nanotag with transmission electron microscopy image of a dye-doped silica-coated Au NP capped with small colloidal Au NPs as shell layer inset at the corner. Copyright (2014) American Chemical Society. Data from [51,68,72,73,77].

The effect of the plasmon-induced local electric field in maximizing SERS enhancement and photothermal ablation is also essential to discuss with some relevant studies. The electric field around NPs directly affects the SERS enhancement factor by generating a first-generation hot spot with moderate intensity. However, the electric field can further be enhanced by changing the structural geometry with sharp corners/tips (e.g., nanowires, NRs, nanoprisms, nanocubes, nanostars, nanodimers, nanotrimers and nanoclusters) because of the lightning rod effect [65]. In addition, the second-generation hot spots originated from coupled nanostructures with optimized subnanometric interparticle separations provide extraordinary intense field confinement for better SERS signaling [66]. By introducing wavy and rough edges or sharp corners to the nanostructures geometry can enhance the SERS signal from two to 12 orders [67]. The SERS signal of rhodamine dye using shape-selective Au nanostructures has been investigated by Kundu *et al.*; they showed that the SERS intensity improves by varying the NPs' shape (i.e., from nanosphere to NR) and to nanoprisms (Figure 4A [I]) [68]. Figure 4A (II) shows the temperature rise by increasing NPs' size and light flux [51]. Further, the shape of anisotropic bipyramid NPs can generate larger SERS enhancement than NRs due to strong local field confinement across the nanoscale tip regions. The bipyramid NPs' LSPR peak width is narrower than NRs' due to smaller plasmon damping [69,70]. Branched NPs (i.e., nanostars and nanoflowers) are the most promising shapes in contrast to other anisotropic nanostructures. The induced plasmons from the central body and from the several arms of the star are coupled and provide better enhancement compared with NRs and nanospheres [71]. With excellent SERS enhancement, Au nanostars also play a promising

role in elevating PTT efficiency with a high light to heat conversion rate. Chatterjee *et al.* [72] studied the impact of nanostar tip sharpness in escalating nearby temperature, as shown in Figure 4B. Simulated electric field strength on nanospike tip head confirms the dependence of field strength on tip sharpness. The heating effect upon laser irradiation (wavelength 785 ± 5 nm) for 20 min shows a maximum rise in temperature (≈30°C) for the sharpest tip heads, causing more cell death. Notably, Lv and coworkers explicitly reported a copper sulfide (CuS)-Au NP system with different morphology and the NPs effect on SERS guided heating during therapy. Figure 4C depicts the structural evolution of hollow core (HC) CuS@islanded Au shell NPs from hollow CuS nanocubes, and their resulting SERS and photothermal effects. The SERS enhancement and photothermal conversion efficiency of HC CuS with spiky Au shell NPs are maximum among these NPs. The real-time monitoring of bio-response assisted by SERS-based intercellular imaging during PTT was successfully achieved due to the plasmonic coupling effect and branched Au tips present on HC-CuS@ spiky Au core-shell configuration [73]. Further, the novel and unique SERS nanotags have emerged as a promising alternative to many traditional plasmonic probes due to their good photostability and ability to provide a strong Raman signal with minimal photobleaching. SERS nanotag (Figure 4D) is composed of metallic NPs, certain Raman reporter molecules and additional encapsulation of a protective shell layer such as silica, ethylene glycol, PEG and bovine serum albumin. Such encapsulation prevents the release of Raman reporter molecules and avoids nonspecific bindings and protein adsorption in the biological environment [74,75]. Jin *et al.* designed the mesoporous silica-coated SERS tags with three different embedded Raman reporters (4-nitrobenzenethiol, benzenedithiol and naphtalenethiol) between the gap of Au nanorod core and Ag shell. Such complex Au@Ag rodlike nanomatryoshkas with embedded Raman reporters have built-in hot spots due to gap-enhanced plasmon coupling effect [76]. In another work, the Halas group reported unique Au rodlike nanomatryoshkas consist of a Au core enclosed by a thin SiO_2 layer, capped with a Au shell layer (Figure 4D). Interestingly the dye molecules are bound within the pores of silica matrix and the strong interaction between the Au core and shell layer gave rise to hybrid plasmon modes with strong NIR absorbance. In such NPs, the reporter molecules are positioned within a few nm of the metallic surface, which can lead to a strong SERS signal with quantitative information [77].

Impact of NP toxicity, biodistribution & surface functionalization

The enhanced permeability and retention effect in solid tumor tissues due to increased vascular permeability could be used to drive NP accumulations in tumor sites compared with normal tissues. Such an inherent characteristic of tumor cells to retain drug-loaded NPs due to the enhanced permeability and retention effect enhances passive targeting. Further, active targeting requires NPs conjugated with antibodies, cytokines, aptamers, peptides or other appropriate targeting ligands that can identify markers of cancer cells. Thus, targeting tumor cells using NPs has the potential to deliver anticancer agents into tumor sites without affecting the normal cells [78]. Despite current advancements in targeted therapy, the off-target toxicity potential of NPs needs more investigation. For example, Au NPs are usually considered to be biocompatible and stable but, upon intravenous administration, Au NPs form protein corona [64] due to the coating of serum protein, which changes NPs' biological identity and inhibits their ability to selectively bind to carcinogenic cells. As a result, off-targeted NPs can induce additional damages to healthy cells during PTT [15]. Further, the use of specific surfactants such as CTAB during NP synthesis is cytotoxic [79]. Therefore, in most cases, for active targeting and to reduce toxicity, functionalization of NPs is needed.

Most plasmonic NPs can be conjugated with PEG, which improves NPs' colloidal stability and biocompatibility and protects the NPs' surface from absorption of serum proteins to avoid protein corona formation. Also, many PEGylated NPs have been approved by the US FDA [80]. Poly(N-isopropylacrylamide) (pNIPAM) is another crosslinked polymer, and its coating on metal NPs enables the entrapment of Raman reporters without specific affinity toward metal NPs due to their porous structures. Nie and coworkers [81] reported the first *in vivo* SERS imaging of a xenograft tumor model using Au nanostars functionalized with both malachite green Raman reporter and thiolated PEG derivatives, and then conjugated with an antibody to target epidermal growth factor receptor (EGFR) on tumor cell surface (Supplementary Figure 2A). Other than polymer coating, encapsulation through a SiO_2 shell improves NPs' biocompatibility and provides functional groups for attachment of ligands such as Raman active molecules [82]. The unique mesoporous nature of SiO_2 facilitates a large surface area for the effective loading of anticancer drugs and their controlled release [83]. Song *et al.* [84] reported hydroxyapatite/mSiO_2-coated Au nanorods with NIR/pH responsiveness. Supplementary Figure 2B shows the drug release from mSiO_2-Gold nanorods (GNRs) doped with doxorubicin (DOX) in an acidic tumor environment. The collapse of the shell layer enhanced the PTT efficiency as well as biodegradability. Yang *et al.* [82] reported another interesting multifunctional

drug release system involving $mSiO_2$-coated Au nanocage fabrication, as presented in Supplementary Figure 2C. A pNIPAM coating was covalently anchored to form Au nanocage@$mSiO_2$@ pNIPAM. Finally, DOX was loaded into the nanosystem by stirring in phosphate buffer. Upon NIR laser irradiation, the Au nanocages can induce an excellent photothermal effect by subsequent collapse of the polymer shell. Finally, the entrapped DOX could be successfully released for the treatment. Other common ligands used to provide biocompatibility and stability are bovine serum albumin [85], liposomes [86], polyvinylpyrrolidone [87], zwitterionic polymer ligands [88], cysteine [89] and phospholipids [90].

Evaluation of NP biodistribution and toxicological effects can be influenced by several factors, such as NP size, shape and surface chemistry. Among them, the size effect is one of the essential factors that has been studied extensively. Studies revealed that Au NPs larger than 50 nm show comparatively less targeted cellular uptake compared with particles of sizes between 5–15 nm [91,92]. Huo *et al.* have demonstrated that Au NPs less than 6 nm effectively enter the nucleus of the cell, whereas slightly larger NPs (10–16 nm) only penetrate through the cell membrane and in the cytoplasm. Thus, smaller NPs are more toxic than NPs of 10 nm or more, as they can enter the nucleus [93]. Further, *in vivo* experiments have revealed that larger NPs (50–250 nm) are found in the blood, liver and spleen areas, whereas NPs smaller than 10 nm are rapidly distributed among all tissues and organs [94]. The toxicity effect due to biodistribution of bare or functionalized NPs, and the subsequent interference with intercellular processes, also plays a major role. Therefore, the possible negative consequences associated with undesired biodistribution inside the body should be dealt with during the design of therapeutic agents.

In vitro & *in vivo* examples of SERS-guided PTT in nanotheranostics

In 2009, Rycenga *et al.* first reported a combined study of photothermal and SERS effects using a single nanoprobe. The SERS analysis of 1-dodecanethiolate-covered Au-Ag nanocages showed a change in the intensity ratio between two strong G and T carbon-carbon stretching Raman bands due to an increase in sample temperature during laser irradiation. They found that the plasmon excitation in Au-Ag nanocages can simultaneously generate EM enhancement for SERS effect and localized heating for the photothermal applications [95]. In the same year, another critical study by the group of Bhatia reported on SERS-coded PEG-Au nanorods for *in vivo* multiplexing for SERS detection and photothermal heating [96]. A novel approach to deep tumor visualization with highly specific tumor margin detection was reported by Kircher *et al.* in 2012, using core/silica shell/Gadolinium (Gd)-coated NPs in mouse glioblastoma models involving triple-modality such as MRI, photoacoustic imaging and Raman imaging. For the first time, this study detected the invasive tumor margins and their macroscopic extensions using Raman signals [97]. Over the past 11 years, various research groups have made tremendous advances across the globe in tumor theranostics. This section of the review summarizes the reported studies related to SERS imaging-guided photothermal cancer therapy since 2009 (see Table 1) and discusses some of the crucial findings and advancements.

Hybrid NPs composed of a combination of different nanomaterials and different chemical compositions have drawn a lot of research interest due to their unique optical properties. In biomedical research, such composite NPs are used as multifunctional platforms; specifically, combining noble metals with metal chalcogenides/oxides can provide multimodal imaging-guided therapeutic applications [121]. In 2010, for the first time, CuS NPs were investigated for photothermal ablation of carcinogenic tumor cells by Li *et al.* [122]. Since then, Cu chalcogenides and their different combinations with Au or Ag NPs have drawn the attention of many research groups. Nonstoichiometric $Cu_{2-x}S$ NPs containing a large number of hole carriers supports NIR absorption and high photothermal effects. Ding and coworkers [52] reported a dual plasmonic Au-Cu_9S_5 nanohybrid with a well-controlled interface to study the plasmon coupling effect due to the collective oscillation of the electron and hole. Interestingly, the coupling between the plasmonic Au core and Cu_9S_5 semiconductor shell of as-prepared NPs shows an enhanced optical absorption cross section with higher photothermal conversion efficiency at the NIR-II region under low laser power. Later, Lv *et al.* [109] reported an aqueous-mediated green synthesis of folic acid-coated Au@$Cu_{2-x}S$ NPs through anion exchange and employed them in *in vivo* tumor-targeted ablation therapy guided by the SERS imaging modality (see Figure 5A [I]). Transmission electron microscopy imaging confirmed the capping of the $Cu_{2-x}S$ shell layer around the Au core, and the simulated electric field profile showed intense electric field confinement due to surface plasmons and excitons, resulting SERS enhancement of embedded dye molecules (see Figure 5A [II]). During *in vivo* study, Au@$Cu_{2-x}S$ NPs showed excellent photothermal transduction ability upon 808 nm laser irradiation (5 min, 0.72 W cm^{-2}) when intravenously injected Au@$Cu_{2-x}S$ NPs (dose of 10.0 mg kg^{-1}) into 4T1 tumor-bearing mice. A temperature rise up to 40° during PTT can be shown in IR thermal images (see Figure 5A [III]). Further, the SERS imaging of the tumor site allowed clear detection of tumor boundaries (Figure 5A

Table 1. Summary of reported literature where plasmonic nanoparticles have been used for surface-enhanced Raman spectroscopy-guided photothermal therapy applications.

Plasmonic NP	Therapy and cancer cell type (in brief)	Treatment dose	Imaging modality	Ref.
PEGylated Au NRs (2009)	*In vitro* and *in vivo,* photothermal therapy, MDA-MB-435 breast cancer cells	810 nm laser (2 W/cm^2 for 5 min)	Infrared thermographic maps with *in vivo* Raman spectra	[96]
Popcorn-shaped Au NPs (2010)	*In vitro*, photothermal therapy, human prostate cancer cell line (LNCaP)	785 nm laser (12.5 W/cm^2 for 30 min)	*In vitro* SERS assay	[98]
MBA/SMART-Au NPs, MBA-Au NPs (2013)	*In vitro*, photothermal therapy, B16 F10 mouse melanoma cells	785 nm laser (19.5 W/cm^2 for 10 min)	Optical microscope and Raman mapping	[99]
Goldnanostar@ Organosilica @Gd-PEG (MGSNs) (2015)	*In vivo*, photothermal therapy, MDA-MB-231 human breast cancer cell tumor-bearing mice	808 nm laser (0.5 W for 5 min)	*In vivo* MRI and SERS imaging	[100]
DOX@GO@AuNRs (2015)	*In vitro* and *in vivo,* chemo-photothermal Therapy, HeLa cells, human cervical cancer cells	808 nm laser (0.5 W/cm^2 for 10 min)	SERS mapping	[101]
GNR-PANI, GNR-PPy (2015)	*In vitro* and *in vivo,* photothermal ablation, A549 (adenocarcinomic human alveolar basal epithelial) cells	808 nm diode laser (2.5 W/cm^2 for 5 min)	NIR SERS imaging	[102]
GO-Au@PANI (2016)	*In vitro* and *in vivo,* chemo-photothermal therapy, 4T1 mammary carcinoma cells	808 nm laser (2.5 W/cm^2)	SERS-fluorescence dual-mode imaging	[103]
AuNR@pMBA@ PDA@Anti-EpCAM (2017)	*In vitro,* real-time photothermal therapy, DU145 prostate cancer tumor cells and U251 glioblastoma tumor cells	785 nm laser (for 5 min)	SERS imaging	[104]
BP-Au NSs (2017)	*In vitro* and *in vivo,* photothermal therapy, 4T1 mammary carcinoma cells	808 nm laser (2 W/cm^2 for 2 min)	*In vivo* SERS monitoring	[105]
Au@Ag core-shell rodlike nanomatryoshkas (2017)	*In vitro,* photothermal therapy, HeLa cells, cervical cancer cells	808 nm CW laser (4 W/cm^2 for 5 min)	SERS imaging	[76]
GNS-ICG-BSA (2017)	*In vitro,* photothermal therapy, U87 glioma cells	808 nm laser (for 5 min)	SERS mapping	[106]
Au NPs and Au NSs (2017)	*In vitro* and *in vivo,* photothermal therapy, 4T1 mammary carcinoma cells	808 nm diode laser (1 W/cm^2 for 10 min)	Raman mapping	[107]
CuS@Spiky Au core-shell NPs (2018)	*In vitro*, photothermal therapy, HeLa cells, human cervical cancer cells	808 nm laser (0.45 W/cm^2 for 5 min)	Label-free SERS intracellular imaging	[73]
4MBA-labeled Au NP (2018)	*In vitro,* plasmonic photothermal therapy, HepG2 cells, human liver cancer cells	532 nm and 785 nm laser (20 mW for 5 min)	Raman mapping	[108]
Au@$Cu_{2-x}S$ core-shell NPs (2019)	*In vitro* and *in vivo,* photothermal therapy, HeLa cells and 4T1 cells	808 nm laser (0.45 W/cm^2 for 15 min)	SERS and photoacoustic imaging	[109]
Aptamer-conjugated Au nanocage/SiO_2 (2019)	*In vitro,* photothermal therapy, MCF-7 breast cancer cells	785 and 808 nm laser (1.5 W/cm^2 for 5 min)	SERS imaging	[110]
Au nanostars (Au-4MBA-RGD) (2019)	*In vitro,* plasmonic photothermal therapy, A549 human lung adenocarcinoma cells	785 nm NIR-I laser (390 mW/cm^2 for 6 min), 1064 nm NIR-II laser (1160 mW/cm^2)	*In vitro* SERS mapping	[111]
Nanoenvelope (ISQ@BSA-AuNC@AuNR@DAC@DR5) (2019)	*In vitro* and *in vivo*, photodynamic, thermal and chemotherapy, A375 human melanoma cells	808 nm laser for 4 min	Raman mapping	[112]
Au@PB NPs (2020)	*In vitro* and *in vivo*, photodynamic and thermal therapy, 4T1 mammary carcinoma cells	808 nm laser (2.0 W/cm^2 for 10 min)	MRI and Raman mapping	[113]
AuNR-AS1411, AuNR-MUC1 (Bioorthogonal SERS Nanotags) (2020)	*In vitro* and *in vivo,* photothermal therapy, MCF-7 breast cancer cells	808 nm NIR laser (0.2 W/cm^2 for 5 min)	SERS mapping	[114]
HA-4-ATP-AuNFs-DOX (2020)	*In vitro* and *in vivo,* photo-chemo-tumor therapy, MDA-MB-231 breast cancer cells	1064 nm NIR-II laser (1 W/cm^2 for 10 min)	Photoacoustic-Raman dual imaging	[60]
Ag@CuS NPs (2021)	*In vitro,* photothermal therapy, HeLa cells	940 nm light for 15 min	SERS mapping	[115]
MnO_2@Au nanoenvelope (2021)	*In vitro,* photothermal therapy, PANC-1 and WI-38 cells	808 nm, 0.25 W for 4 min	SERS mapping	[116]
HAuNP@DTTC (2021)	*In vitro* and *in vivo,* photothermal therapy, 4T1 cells	808 nm laser for 5 min	SERS mapping	[117]
Au-Ur@DTTC (2021)	*In vitro* and *in vivo,* surgery + adjuvant photothermal therapy, SKOV3 and CT26 tumor	785 nm laser (150 mW for 3–10 min)	Raman imaging	[118]

BSA: Bovine serum albumin; DOX: Doxorubicin; NIR: Near-infrared; NIR-I: First biological window; NIR-II: Second biological window; NP: Nanoparticle; NR: Nanorod; NS:Nanostars ; SERS: Surface-enhanced Raman spectroscopy.

Table 1. Summary of reported literature where plasmonic nanoparticles have been used for surface-enhanced Raman spectroscopy-guided photothermal therapy applications (cont.).

Plasmonic NP	Therapy and cancer cell type (in brief)	Treatment dose	Imaging modality	Ref.
Apt-Ce6-PDA@Pt (2022)	*In vivo* photothermal therapy + photodynamic therapy, HepG2 and GPC3-positive tumor cells	808 nm laser (2.0 W/cm^2 for 5 min)	Raman mapping and real-time fluorescence imaging	[119]
AuDAg$_2$s (2022)	*In vitro* and *in vivo*, photothermal therapy, CT26 colon tumor cells	1064 nm laser irradiation (0.5 W/cm^2 for 5 min)	SERS/NIR-II multidimensional tumor imaging	[120]

BSA: Bovine serum albumin; DOX: Doxorubicin; NIR: Near-infrared; NIR-I: First biological window; NIR-II: Second biological window; NP: Nanoparticle; NR: Nanorod; NS:Nanostars ; SERS: Surface-enhanced Raman spectroscopy.

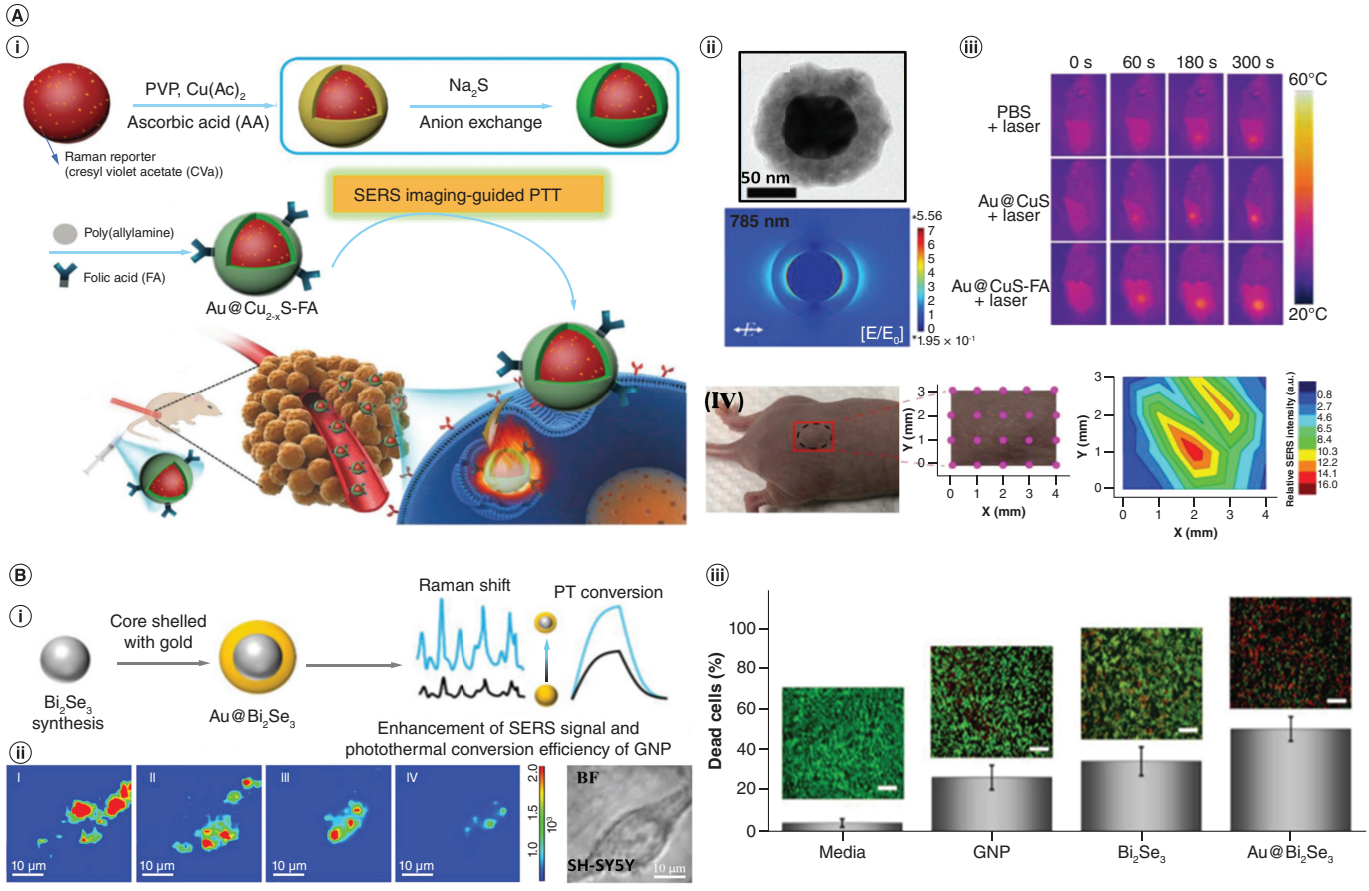

Figure 5. Noble metals with metal chalcogenides/oxides for SERS imaging-guided PTT applications. (A) (I) Schematic of Au@$Cu_{2-x}S$ synthesis route and their *in vivo* application using surface-enhanced Raman spectroscopy (SERS)-guided photothermal therapy. **(II)** Au@$Cu_{2-x}S$ nanoparticles (NPs) transmission electron microscopy image and the simulated electric field profile at 785 nm excitation. **(III)** Infrared thermal image of mice during photothermal therapy under 808 nm laser irradiation (5 min; 0.72 W cm^{-2}) with different treatment conditions. **(IV)** Photograph of tumor-bearing mice with SERS detection points are represented by pink dots and the corresponding SERS contour image. Copyright (2018), John Wiley and Sons. **(B) (I)** Schematic illustration of the synthesis of Au@Bi_2Se_3 NPs. **(II)** Raman mapping of antagomiR-152 strand displacement and release in SH-SY5Y cells by oncomiR-152. **(III)** SH-SY5Y cells' death rate after internalization of different unmodified NPs under 808 nm laser (6 min; 2 W cm^{-2}) irradiation. Copyright (2018), John Wiley and Sons. Data from [109,125].

[IV]) and helped navigate the excision of NPs. In this context, considering higher SERS enhancement due to Ag NPs compared with Au, recently the authors' group synthesized dual plasmonic Ag@CuS core-shell NPs using a simple, self-limiting hydrothermal route. They have exhibited not only strong NIR absorbance but also strong SERS enhancement with good biocompatibility and photostability when applied *in vitro* using HeLa cells, which confirms their potential SERS-guided PTT efficiency [115]. The economic and simple synthesis process of such metal@semiconductor nanoprobes with a broader absorbance range allows flexibility in choosing light sources

during therapy. The use of newly developed Bi_2Se_3 has shown the potential for many clinical applications such as diagnosis, imaging and radiation therapy. Under light excitation, the Dirac surface state plasmons due to spin density wave oscillation and then the net spin polarization makes Bi_2Se_3 a unique plasmonic material [123,124]. Recently, the Choi group [125] synthesized bifunctional Au@Bi_2Se_3 core-shell NPs (Figure 5B [I]). The hybrid system of Au shell around Bi_2Se_3 NPs improves the SERS signal twofold compared with pure Au NPs, and the photothermal conversion efficiency also increases to 35.5%, which is 1.8-times larger than pure Au NPs. Their small size (≈11 nm) allows passive accumulation at the tumor site. Later, they functionalized the Au@Bi_2Se_3 NPs' surface with polyvinylpyrrolidone, folic acid conjugated with cell-penetrating peptide (CPP) and CY3.5-modified antagomiR-152 to study the oncomiR detection through strand displacement of antagomiR-152 and inhibition. Raman mapping of the process of antagomiR-152 strand displacement and release in SH-SY5Y cells by oncomiR-152 can be seen in Figure 5B (II). Under identical experimental conditions, the PTT results of SH-SY5Y cells after incubation with Au NPs, Bi_2Se_3 NPs and Au@Bi_2Se_3 NPs are represented in Figure 5B (III); a maximum of 52% of cell death was recorded for cells treated with Au@Bi_2Se_3 NPs. Such dual-functioning NPs can provide a deeper insight into PTT-induced cell death from a molecular perspective, which can be used for real-time monitoring of biochemical response during and after the treatment.

Redox active transition metal-dioxides such as MnO_2 and its composites have recently been applied as a new therapeutic material due to their extraordinary performance in cancer theranostics. These nanomaterial's large surface area can offer high drug loading and delivery efficiencies. Due to the strong catalytic and oxidative nature of MnO_2, it can be reduced to Mn^{4+} in the presence of certain reducing substances such as glutathione or H_2O_2. Interestingly, the concentration of such reducing agents is higher in carcinogenic cells than in normal cells. Thus, MnO_2 can be reduced to Mn^{4+} and their degradation process achieved through the specific release of loaded drugs during treatment [126–128]. Recently, Maiti and coworkers [116] reported a new CCK peptide-conjugated MnO_2@AuNP system, named photothermal theranostic nanoenvelope for real-time monitoring of SERS-guided PTT (Figure 6A [I]). In this system, the degradation of the MnO_2 layer in the presence of H_2O_2 inside malignant cells enables real-time tracking of temperature-induced intercellular changes. The PTT caused selective degradation of the MnO_2 shell layer of the NPs; consequently, the exposure of Au cores inside the intercellular region has been used to get vital information of biomolecular changes. Live-dead assay of PANC-1 cells before and after PTT using 808 nm laser for 4 min further confirmed the cell apoptosis under different treatments (Figure 6B [II]). The percentage of dead cells was highest when treated with photothermal theranostic nanoenvelope. The SERS mapping of pancreatic PANC-1 cells and corresponding spectra collected before and after PTT are shown in Figure 6B (II). The absence of IR peaks at 832 and 1210 cm^{-1} and the presence of a 1523 cm^{-1} peak (N_7-H band from nucleic bases) confirms the temperature-induced apoptotic cell death (Figure 6A [III]) [129]. The NIR-II bio-window (1000–1350 nm) is very useful, as it enables MPE and deep tissue penetration during *in vivo* experiments. Therefore, the designing of NIR-II active nanoprobes holds excellent promise for phototheranostic applications. Apart from nanocomposites, smart structural engineering can make typical Au NPs into advanced, multifunctional therapeutic probes to use in the NIR-II bio-window region. Recently, Wang *et al.* [60] fabricated a new kind of mesoporous-based Au NP grafted by hyaluronic acid (HA-4-ATP-AuNF), which acted as a capping agent for loaded DOX within mesopores and improved the biocompatibility of the NPs (Figure 6B [I]). The presence of a large number of hot spots in Au NFs enhanced the Raman imaging with amplified fingerprints at 1085 cm^{-1} and 1585 cm^{-1} (Figure 6B [II]). More interestingly, it has an excellent photothermal effect in the NIR-II region and can release DOX molecules efficiently during therapy (Figure 6B [III]). Also, due to high absorbance, their photostability and photothermal efficiency have been improved. The IR thermal image of MDA-MB-231 tumor-bearing mice under 1064 nm laser irradiation (1 W cm^{-2}) for 10 min after intravenous injection of HA-4-ATP-AuNFs with phosphate-buffered saline shows a maximum rise in temperature (≈20°C) across the tumor region (Figure 6B [IV]). *In vivo* chemo-phototherapy using DOX-loaded HA-4-ATP-AuNFs upon NIR-II laser irradiation resulted in complete removal of the tumor from the target site. It can serve as a multimodal imaging platform through photoacoustic–SERS dual-imaging modes. Collectively, Au NFs are highly multifunctional, making them a potential theranostic agent for future clinical translation.

During surgery and phototherapy, precise and accurate detection of the tumor core, tumor margins and microscopic extensions is extremely important. Failure to complete tumor ablation through PTT or resection through surgery can be lethal due to tumor reoccurrence and metastasis. Approximately 80–90% of the recurrence of glioblastomas in patients is initiated from the residual microtumors [130]. Thus, developing an intraoperative, non-invasive optical imaging approach to detect residual tumors decreases the chances of reoccurrence. To mitigate the

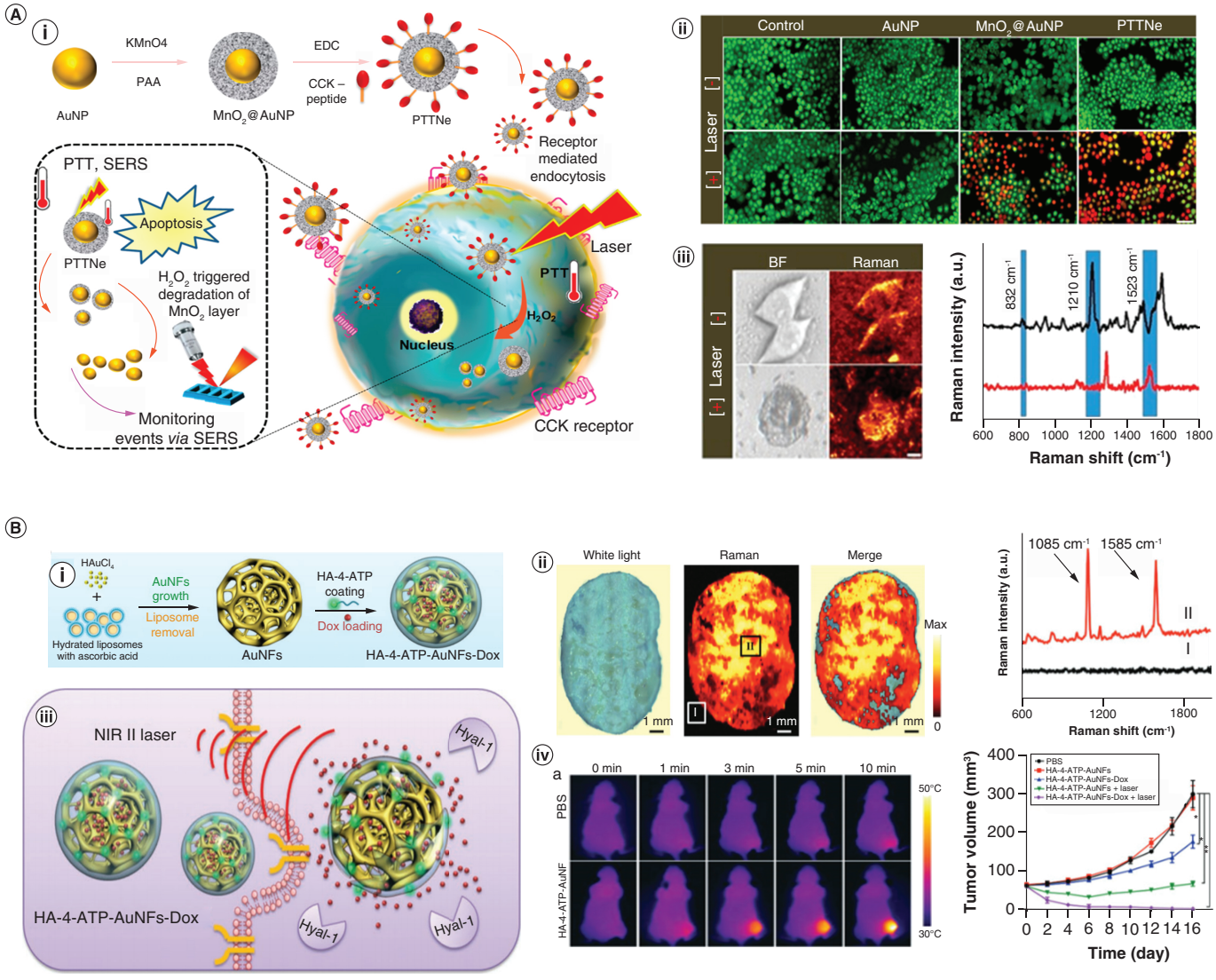

Figure 6. Redox active transition metal-dioxides and mesoporous metal nanostuctures for SERS guided PTT application. (A) (I) Schematic representation of MnO_2@AuNPs as surface-enhanced Raman spectroscopy (SERS)-guided photothermal therapy (PTT) probe for pancreatic cancer. **(II)** Live-dead cell assay with viability results of PANC-1 cells with and without laser irradiation under different treatment conditions. **(III)** Raman mapping of PANC-1 cells and corresponding SERS spectra before and after PTT. Copyright (2021) American Chemical Society. **(B) (I)** Synthesis scheme of doxorubicin-loaded HA-4-ATP-AuNFs. **(II)** *In vivo* SERS mapping of the tumor tissue with 785 nm laser excitation. Colors represent the characteristic Raman band intensity of HA-4-ATP-AuNFs at 1585 cm^{-1} and corresponding two recorded Raman spectra from points I and II. **(III)** Release of doxorubicin during PTT in the second biological window. **(IV)** Infrared images of tumor-bearing mice under 1064 nm laser irradiation (1 W cm^{-2}) for 10 min after intravenous injection with phosphate-buffered saline and HA-4-ATP-AuNFs, respectively, and the tumor volume growth curve of mice with respect to time under different treatments. Copyright (2020), John Wiley and Sons. Data from [60,116].

issue of reoccurrence, SERS-based imaging-guided therapy and surgery are being developed and drawing attention due to their high resolution, sensitivity, specificity and ability to provide signature signals [131]. Interestingly, Kircher and coworkers first reported near real-time SERS detection and static imaging using Au@SiO_2 NPs with a handheld Raman scanner, targeting glioblastoma tissues on a genetically engineered mouse model in an intra-operative situation [132]. Another report from the same group showed improved identification of tumor margins using Au nanostars instead of silica-coated Au nanospheres [133]. Zhu *et al.* [113] investigated the potential use of monodispersed Prussian blue-capped Au NPs (Au@PB@HA NPs) for dual-mode imaging (SERS/MRI)-guided phototherapy (Figure 7A [I]). The negatively charged as-prepared NPs reduced their nonspecific interaction with normal tissues and serum proteins. After intravenous injection of NPs, the SERS imaging modality can provide

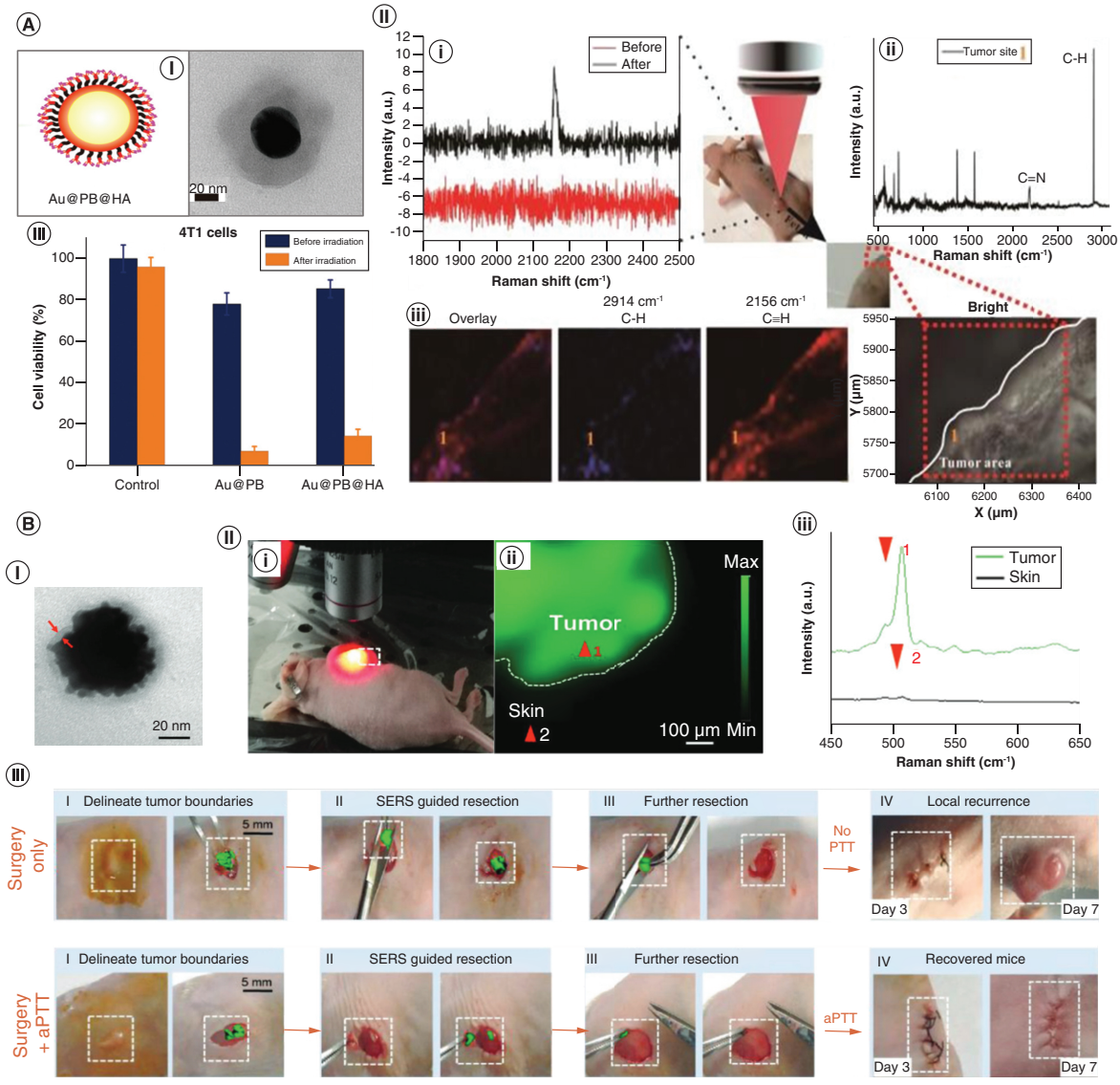

Figure 7. Tumour margin identification and treatment using SERS imaging guided PTT. (A) (I) Schematic illustration and transmission electron microscopy image of plasmonic Au@PB@HA nanoparticles (NPs). **(II)** *In vivo* Raman imaging of 4T1 tumor-bearing mice. (i) Recorded Raman band at 2156 cm^{-1}. (ii) Raman spectrum with no background interference was collected after intravenous injection of Au@PB@HA NPs. (iii) Raman mapping of the tumor tissue, where red and blue colors are assigned for characteristic Raman band of Au@PB@HA NPs at 2156 cm^{-1} and 2914 cm^{-1}, respectively. **(III)** 4T1 cell viability before and after treatment under 808 nm laser irradiation at 200 μg ml^{-1} NP concentration. Copyright (2020), Royal Society of Chemistry. **(B) (I)** Transmission electron microscopy image of Au-Ur@DTTC NPs. **(II)** (i) Photograph of subcutaneous SKOV3 tumor-bearing mouse. (ii) Raman image of the tumor. (iii) The corresponding Raman signal within (red arrow 1) and nearby skin (red arrow 2). **(III)** Raman imaging-assisted surgery and surgery with adjuvant photothermal therapy under 785 nm laser (150 mW) for 3–10 min of irradiation. Data from [113,118].

distinct SERS emission from tumor and nontumor parts (Figure 7A [II]). No signal interference was observed from natural components of the tumor in the Raman silent region. *In vitro* cytotoxicity assay by comparing before and after PTT decreased the viability of 4T1 cells to below 10% after 10 min, 808 nm laser irradiation using 200 μg mL^{-1} NP concentration (Figure 7A [III]). The reported NPs also showed long blood circulation time with excellent biocompatibility. Recently, the Zhou group [118] reported a critical study focused on SERS imaging-assisted tumor margin ablation through PTT. Synthesized diethylthiatricarbocyanine iodide (DTTC)-tagged Au nanourchin (Au-Ur@DTTC; Figure 7B [I]) Raman activity was investigated through Raman imaging of subcutaneous SKOV3 and CT26 tumors. Compared with nearby skin tissues, the tumor site showed a significantly high Raman signal

(Figure 7B [II]) which confirms the NPs' tumor detection ability through Raman imaging. They evaluated Au-Ur@DTTC NPs for intraoperative Raman imaging-guided resection of subcutaneous SKOV3 ovarian tumors and postsurgical PTT to eliminate residual tumor margins (Figure 7B [III]). After surgery followed by adjuvant PTT under 785 nm laser (150 mW; 3–10 min) showed a complete removal of the tumor with no more SERS signals, with a lower reocurrence rate during a 36-day monitoring period as compared with only surgery. Further, the NPs' *in vivo* toxicity, biodistribution and pharmacokinetic study results also validated their clinical translatability.

Conclusion

In summary, SERS-guided PTT is a potential option for cancer diagnostics and therapy. In this review, we have discussed the SERS and PT effect of plasmonic nanocomposites and highlighted the impact of various influential factors such as the size, shape and surface chemistry of NPs. This review also provides details of recent developments, particularly in the field of SERS imaging-guided PTT. The new class of plasmonic NPs provides information on intratumoral heterogeneity and tumor margins via SERS imaging using NIR laser, both regions I and II. Localized plasmon heating selectively increases the tumor temperature to establish photothermal-induced cell apoptosis. Multifunctional plasmonic nanoprobes are a powerful next generation of nanomedicine for cancer diagnosis via real-time monitoring of temperature-induced cell death under low-power NIR laser irradiation without causing harmful effects to normal cells.

Future perspective

Despite the considerable progress that has been achieved in the field of dual-functioning plasmonic NPs for theranostic purposes, it is still at the preliminary stage from the standpoint of human trials. For clinical translation, several challenges need to be addressed. More studies for NPs' long-term biosafety, toxicity and successful excretion from the body after therapy need to be completed before any clinical trial using humans. A short-term *in vivo* animal study is not sufficient to prove any irreversible genetic changes after therapy due to continuous exposure to NPs. Further, nonspecific biodistribution and low accumulation of NPs at targeted areas can reduce treatment efficacy remarkably. Also, it is very difficult for the NPs to go deeper into the solid tumors, which severely limits their PTT effectiveness. Designing plasmonic NPs with LSPR band in NIR-II can reduce fluorescence background and improve tissue penetration depth. Furthermore, employing light-emitting diodes as light sources during PTT has shown therapeutic effects comparable to those of low-intensity lasers and can be used as a safer and cheaper alternative to targeting large surface areas [134].

Still, in oncological studies the detection and imaging of deep tumors using SERS NPs demand high-quality deep tissue Raman detectors, which is another promising future task for researchers. Implementation of an optical fiber-guided SERS imaging tool, Raman endoscopy or colonoscopy to detect superficial tumor tissues in the body itself could accelerate the applicability in the near future. Consequently, designing multifunctional plasmonic probes with the benefits of enhanced SERS imaging, drug loading, photothermal capability and long-term stability in biological systems, as well as excellent biocompatibility, is essential for any real-life, practical application. Further, the future success of oncological phototherapies using plasmonic NPs and their fast clinical translations mostly rely on advanced electro-optic properties and their smart structural engineering. We believe with continuous endeavor and with close collaborations among clinicians and researchers, we could design a multifunctional plasmonic nanotheranostic agent that can serve as an alternative to many invasive oncological treatments and that has huge potential for clinical translation.

Supplementary data

To view the supplementary data that accompany this paper please visit the journal website at: www.futuremedicine.com/doi/suppl/10.2217/nnm-2023-0010

Author contributions

A Das designed the study and wrote the first draft of the manuscrift. H-C Tsai edited and reviewed the draft. RS Moirangthem and T Sen critically revised and edited the paper. All authors contributed to manuscript revision and read and approved the submitted version.

Executive summary

Background

- Surface-enhanced Raman spectroscopy (SERS)-guided plasmonic photothermal therapy (PTT) has emerged as a noninvasive technique that is capable of overcoming the major limitations of traditional oncotherapy.
- Plasmonic nanostructure-mediated Raman signal enhancement and photothermal heating mechanisms are discussed, considering both electromagnetic and two-temperature model theories.

Influencing factors in nanoparticle design to achieve improved therapeutic efficacy

- The composition, shape and size of nanoparticles (NPs) and their associated physicochemical properties are critical factors that determine their efficiency in tumor accumulation, retention and SERS imaging ability.
- Surface functionalization provides NPs colloidal stability and biocompatibility and protects the NPs' surface from absorption of serum proteins to avoid protein corona formation.
- The importance of site-specific delivery, along with minimal or no toxicological effect and undesired biodistribution inside the body, should be the prime focus of engineered nanotherapeutic agents.

SERS-guided PTT in nanotheranostics

- A close examination of the latest studies on SERS imaging-guided PTT indicates a significant advancement in nanotheranostics by exploiting engineered plasmonic NPs.
- Multifunctional plasmonic nanoprobes are potentially the next generation of nanomedicine for the diagnosis of cancer via real-time monitoring of temperature-induced cell death under near-infrared laser irradiation without affecting healthy tissues.
- Faster clinical translation relies on advanced electro-optic properties and their smart structural engineering.

Conclusion & future perspective

- SERS-guided PTT is a potential option for cancer diagnostics and therapy.
- The technique provides important information on intratumoral heterogeneity and tumor margins via SERS imaging using near-infrared laser in regions I and II.
- Close collaborations among clinicians and researchers is needed to design a multifunctional plasmonic nanotheranostic agent that can serve as an alternative to many invasive oncological treatments.

Financial & competing interests disclosure

A Das and RS Moirangthem would like to acknowledge financial support from the Science and Engineering Research Board (SERB-DST), India (EEQ/2017/000370). The authors have no other relevant affiliations and financial involvement with any organization or entity with a financial interest in or financial conflict with the subject matter or materials discussed in the manuscript apart from those disclosed.

No writing assistance was utilized in the production of this manuscript.

Editorial board disclosure

T Sen is a member of the *Nanomedicine* Editorial Board. They were not involved in any editorial decisions related to the publication of this article, and all author details were blinded to the article's peer reviewers as per the journal's double-blind peer review policy.

References

Papers of special note have been highlighted as: • of interest; •• of considerable interest

1. Zou L, Wang H, He B *et al.* Current approaches of photothermal therapy in treating cancer metastasis with nanotherapeutics. *Theranostics* 6(6), 762 (2016).
2. Wan L, Pantel K, Kang Y. Tumor metastasis: moving new biological insights into the clinic. *Nat. Med.* 19(11), 1450–1464 (2013).
3. Verma SS. Plasmonics in nanomedicine: a review. *Glob. J. Nano* 4(5), 2573–2374 (2018).
4. Fratila RM, de la Fuente JM (Eds.). *Nanomaterials for Magnetic and Optical Hyperthermia Applications.* Elsevier, (2018).
5. Zheng YB, Kiraly B, Weiss PS, Huang TJ. Molecular plasmonics for biology and nanomedicine. *Nanomedicine* 7(5), 751–770 (2012).
6. Liu J, He H, Xiao D *et al.* Recent advances of plasmonic nanoparticles and their applications. *Materials* 11(10), 1833 (2018).
7. Maier SA. *Plasmonics: Fundamentals and Applications.* Springer, New York, NY, USA (2007).
8. Richardson NV, Holloway S. (Ed.) The basics of plasmonics. In: *Handbook of Surface Science (Volume 4).* Elsevier, North-Holland, 37–74 (2014).
9. Mayer KM, Hafner JH. Localized surface plasmon resonance sensors. *Chem. Rev.* 111(6), 3828–3857 (2011).
10. Enoch S, Bonod N. In: *Plasmonics – from Basics to Advanced Topics (Volume 167).*Springer, NY USA, 1534–1556 (2012).
11. Wei H, Xu H. Plasmonics in composite nanostructures. *Mater. Today* 17(8), 372–380 (2014).

12. Yaremchuk IY. Optical properties of nanocomposite materials based on plasmon nanoparticles. *Semicond. Phys. Quantum Electron. Optoelectron.* 21(2), 195–199 (2018).
13. Pastoriza-Santos I, Kinnear C, Pérez-Juste J, Mulvaney P, Liz-Marzán LM. Plasmonic polymer nanocomposites. *Nat. Rev. Mater.* 3(10), 375–391 (2018).
14. Shanmugam V, Selvakumar S, Yeh CS. Near-infrared light-responsive nanomaterials in cancer therapeutics. *Chem. Soc. Rev.* 43(17), 6254–7287 (2014).
15. Riley RS, Day ES. Gold nanoparticle-mediated photothermal therapy: applications and opportunities for multimodal cancer treatment. *Wiley Interdiscip. Rev. Nanomed. Nanobiotechnol.* 9(4), e1449 (2017).
16. Chen F, Cai W. Nanomedicine for targeted photothermal cancer therapy: where are we now? *Nanomedicine* 10(1), 1–3 (2015).
17. Kim M, Lee JH, Nam JM. Plasmonic photothermal nanoparticles for biomedical applications. *Adv. Sci.* 6(7), 1900471 (2019).
18. Khan I, Saeed K, Khan I. Nanoparticles: properties, applications and toxicities. *Arab. J. Chem.* 12(7), 908–931 (2019).
19. Lal S, Clare SE, Halas NJ. Nanoshell-enabled photothermal cancer therapy: impending clinical impact. *Acc. Chem. Res.* 41(12), 1842–1851 (2008).
20. (Ed.). *Raman Spectroscopy for Soft Matter Applications.* Amer M, John Wiley & Sons (2008).
21. Hillman EMC, Amoozegar CB, Wang T *et al. In vivo* optical imaging and dynamic contrast methods for biomedical research, Philosophical Transactions of the Royal Society A: mathematical. *Phys. Eng. Sci.* 369(1955), 4620–4643 (2011).
22. Bohn S, Sperlich K, Allgeier S *et al.* Cellular *in vivo* 3D imaging of the cornea by confocal laser scanning microscopy. *Biomed. Opt. Express* 9(6), 2511 (2018).
23. Tipping WJ, Lee M, Serrels A, Brunton VG, Hulme AN. Stimulated Raman scattering microscopy: an emerging tool for drug discovery. *Chem. Soc. Rev.* 45(8), 2075–2089 (2016).
24. Petibois C, Desbat B. Clinical application of FTIR imaging: new reasons for hope. *Trends Biotechnol.* 28(10), 495–500 (2010).
25. Abramczyk H, Brozek-Pluska B. Raman imaging in biochemical and biomedical applications. Diagnosis and treatment of breast cancer. *Chem. Rev.* 113(8), 5766–5781 (2013).
26. Barhoumi A, Zhang D, Tam F, Halas NJ. Surface-enhanced raman spectroscopy of DNA. *J. Am. Chem. Soc.* 130(16), 5523–5529 (2008).
27. Sivanesan A, Izake EL, Agoston R, Ayoko GA, Sillence M. Reproducible and label-free biosensor for the selective extraction and rapid detection of proteins in biological fluids. *J. Nanobiotechnology* 13(1), 1–7 (2015).
28. Henry AI, Sharma B, Cardinal MF, Kurouski D, Van Duyne RP. Surface-enhanced Raman spectroscopy biosensing: *in vivo* diagnostics and multimodal imaging. *Anal. Chem.* 88(13), 6638–6647 (2016).
29. Fratila RM, De La Fuente JM. Noble metal-based plasmonic nanoparticles for SERS imaging and photothermal therapy. In: *Nanomaterials for Magnetic and Optical Hyperthermia Applications.* Elsevier , 83–109 (2018).
30. Li Y, Wei Q, Ma F, Li X, Liu F, Zhou M. Surface-enhanced Raman nanoparticles for tumor theranostics applications. *Acta Pharm. Sin. B* 8(3), 349–359 (2018).
31. Liu M, Anderson RC, Lan X, Conti PS, Chen K. Recent advances in the development of nanoparticles for multimodality imaging and therapy of cancer. *Med. Res. Rev.* 40(3), 909–930 (2020).
32. Cialla-May D, Zheng XS, Weber K, Popp J. Recent progress in surface-enhanced Raman spectroscopy for biological and biomedical applications: from cells to clinics. *Chem. Soc. Rev.* 46(13), 3945–3961 (2017).
33. Huang Z, Zhang A, Zhang Q, Cui D. Nanomaterial-based SERS sensing technology for biomedical application. *J. Mater. Chem. B* 7(24), 3755–3774 (2019).
34. Le Ru EC, Etchegoin PG. Principles of surface-enhanced Raman Spectroscopy. In: *Principle and Clinical Diagnostic Applications of Surface-Enhanced Raman Spectroscopy.* Elsevier, UK 1–32 (2009).
35. Wokaun A. Surface-enhanced electromagnetic processes. *Solid State Phys.* 38(C), 223–294 (1984).
36. Guillot N, de la Chapelle ML. The electromagnetic effect in surface enhanced Raman scattering: enhancement optimization using precisely controlled nanostructures. *J. Quant. Spectrosc. Radiat. Transf.* 113(18), 2321–2333 (2012).
37. Xie Y, Wu DY, Liu GK *et al.* Adsorption and photon-driven charge transfer of pyridine on a cobalt electrode analyzed by surface enhanced Raman spectroscopy and relevant theories. *J. Electroanal. Chem.* 554-555(1), 417–425 (2003).
38. Stiles PL, Dieringer JA, Shah NC, Van Duyne RP. Surface-enhanced Raman spectroscopy. *Annu. Rev. Anal. Chem.* 1, 601–626 (2008).
39. Le Ru EC, Etchegoin PG. Rigorous justification of the |E|4 enhancement factor in surface enhanced Raman spectroscopy. *Chem. Phys. Lett.* 423(1-3), 63–66 (2006).
40. Campion A, Kambhampati P, Campion A, Harris C. Surface-enhanced Raman scattering. *Chem. Soc. Rev.* 27, 241–250 (1998).
41. Le Ru EC, Etchegoin PG. Quantifying SERS enhancements. *MRS Bull.* 38(8), 631–640 (2013).

42. Kim J, Jang Y, Kim NJ *et al.* Study of chemical enhancement mechanism in non-plasmonic surface enhanced Raman spectroscopy (SERS). *Front. Chem.* 7, 582 (2019).

43. Fleischmann M, Hendra PJ, McQuillan AJ. Raman spectra of pyridine adsorbed at a silver electrode. *Chem. Phys. Lett.* 26(2), 163–166 (1974).

44. King FW, Van Duyne RP, Schatz GC. Theory of Raman scattering by molecules adsorbed on electrode surfaces. *J. Chem. Phys.* 69(10), 4472–4481 (1978).

45. Li X, Xiao D, Zhang Z. Landau damping of quantum plasmons in metal nanostructures. *New J. Phys.* 15(2), 023011 (2013).

46. Brongersma ML, Halas NJ, Nordlander P. Plasmon-induced hot carrier science and technology. *Nat. Nanotechnol.* 10(1), 25–34 (2015).

47. Qiu TQ, Tien CL. Short-pulse laser heating on metals. *Int. J. Heat Mass Transf.* 35(3), 719–726 (1992).

48. Kuppe C, Rusimova KR, Ohnoutek L, Slavov D, Valev VK. "Hot" in plasmonics: temperature-related concepts and applications of metal nanostructures. *Adv. Optic. Mater.* 8(1), 1901166 (2020).

49. Li J, Yang J, Gu X. The distribution of absorptive power dissipation in irradiated nanoparticulate system. *J. Quant. Spectrosc. Radiat. Transf.* 182, 102–111 (2016).

50. Govorov AO, Zhang W, Skeini T, Richardson H, Lee J, Kotov NA. Gold nanoparticle ensembles as heaters and actuators: melting and collective plasmon resonances. *Nanoscale Res. Lett.* 1(1), 84–90 (2006).

51. Govorov AO, Richardson HH. Generating heat with metal nanoparticles. *Nano Today* 2(1), 30–38 (2007).

52. Ding X, Liow CH, Zhang M *et al.* Surface plasmon resonance enhanced light absorption and photothermal therapy in the second near-infrared window. *J. Am. Chem. Soc.* 136(44), 15684–15693 (2014).

53. Toy R, Peiris PM, Ghaghada KB, Karathanasis E. Shaping cancer nanomedicine: the effect of particle shape on the *in vivo* journey of nanoparticles. *Nanomedcine* 9(1), 121–134 (2014).

54. Sharma B, Frontiera RR, Henry AI, Ringe E, Van Duyne RP. SERS: materials, applications, and the future. *Mater. Today* 15(1-2), 16–25 (2012).

55. Yang Z, Sun Z, Ren Y *et al.* Advances in nanomaterials for use in photothermal and photodynamic therapeutics. *Mol. Med. Rep.* 20(1), 5–15 (2019).

56. Du Z, Qi Y, He J, Zhong D, Zhou M. Recent advances in applications of nanoparticles in SERS *in vivo* imaging. *Wiley Interdiscip. Rev. Nanomed. Nanobiotechnol.* 13(2), e1672 (2020).

57. Doughty ACV, Hoover AR, Layton E, Murray CK, Howard EW, Chen WR. Nanomaterial applications in photothermal therapy for cancer. *Materials* 12(5), 779 (2019).

58. Rosal B, Haro-Gonzalez P, Benayas A. Nanoparticles for photothermal therapies. *Nanoscale* 6(16), 9494–9530 (2014).

59. Bhattacharjee G, Majumder S, Senapati D, Banerjee S, Satpati B. Core-shell gold @silver hollow nanocubes for higher SERS enhancement and non-enzymatic biosensor. *Mater. Chem. Phys.* 239, 122113 (2020).

60. Wang J, Sun J, Wang Y *et al.* Gold nanoframeworks with mesopores for Raman-photoacoustic imaging and photo-chemo tumor therapy in the second near-infrared biowindow. *Adv. Funct. Mater.* 1908825, 1–13 (2020).

- **Functionalized gold nanoframeworks near infrared region(NIR)-II was used for *in vivo* photothermal therapy and multimodal imaging applications. Greater maximum permissible exposure and deeper tissue penetration also achieved in this study.**

61. Abadeer NS, Brennan MR, Wilson WL, Murphy CJ. Distance and plasmon wavelength dependent fluorescence of molecules bound to silica-coated gold nanorods. *ACS Nano* 8(8), 8392–8406 (2014).

62. Barbosa S, Agrawal A, Rodríguez-Lorenzo L *et al.* Tuning size and sensing properties in colloidal gold nanostars. *Langmuir* 26(18), 14943–14950 (2010).

63. Zhu H, Wang Y, Chen C *et al.* Monodisperse dual plasmonic Au@Cu_{2-x}E (E=S, Se) core@shell supraparticles: aqueous fabrication, multimodal imaging, and tumor therapy at *in vivo* level. *ACS Nano* 11(8), 8273–8281 (2017).

64. Blanco E, Shen H, Ferrari M. Principles of nanoparticle design for overcoming biological barriers to drug delivery. *Nature Biotechnol.* 33(9), 941–951 (2015).

65. Fukuoka N, Tanabe K. Lightning-rod effect of plasmonic field enhancement on hydrogen-absorbing transition metals. *Nanomaterials* 9(9), 1235 (2019).

66. Wang AX, Kong X. Review of recent progress of plasmonic materials and nano-structures for surface-enhanced Raman scattering. *Materials (Basel)* 8(6), 3024–3052 (2015).

67. Yang Y, Zhong XL, Zhang Q *et al.* The role of etching in the formation of Ag nanoplates with straight, curved and wavy edges and comparison of their SERS properties. *Small* 10(7), 1430–1437 (2014).

68. Kundu S. A new route for the formation of Au nanowires and application of shape-selective Au nanoparticles in SERS studies. *J. Mater. Chem. C* 1(4), 831–842 (2013).

69. Li Q, Zhuo X, Li S, Ruan Q, Xu QH, Wang J. Production of monodisperse gold nanobipyramids with number percentages approaching 100% and evaluation of their plasmonic properties. *Adv. Opt. Mater.* 3(6), 801–812 (2015).

70. Chow TH, Li N, Bai X, Zhuo X, Shao L, Wang J. Gold nanobipyramids: an emerging and versatile type of plasmonic nanoparticles. *Acc. Chem. Res.* 52(8), 2136–2146 (2019).

71. Xu M, Zhang J,Precisely controllable synthesized nanoparticles for surface enhanced Raman spectroscopy. In: *Raman Spectroscopy.* Nascimento GD, InTech (2018).

72. Chatterjee H, Rahman DS, Sengupta M, Ghosh SK. Gold nanostars in plasmonic photothermal therapy: the role of tip heads in the thermoplasmonic landscape. *J. Phys. Chem. C* 122(24), 13082–13094 (2018).

73. Lv Q, Gao MY, Cheng ZH, Chen Q, Shen AG, Hu JM. Rational synthesis of hollow cubic CuS@Spiky Au core-shell nanoparticles for enhanced photothermal and SERS effects. *Chem. Commun.* 54(95), 13399–13402 (2018).

74. Wang Y, Yan B, Chen L. SERS tags: novel optical nanoprobes for bioanalysis. *Chem. Rev.* 113(3), 1391–1428 (2013).

75. Guerrini L, Pazos-Perez N, Garcia-Rico E, Alvarez-Puebla R. Cancer characterization and diagnosis with SERS-encoded particles. *Cancer Nanotechnol.* 8, 1–24 (2017).

76. Jin X, Khlebtsov BN, Khanadeev VA, Khlebtsov NG, Ye J. Rational design of ultrabright SERS probes with embedded reporters for bioimaging and photothermal therapy. *ACS Appl. Mater. Interfaces* 9(36), 30387–30397 (2017).

77. Ayala-Orozco C, Liu JG, Knight MW *et al.* Fluorescence enhancement of molecules inside a gold nanomatryoshka. *Nano Lett.* 14(5), 2926–2933 (2014).

78. Singh S, Sharma A, Robertson GP. Realizing the clinical potential of cancer nanotechnology by minimizing toxicologic and targeted delivery concerns. *Cancer Res.* 72(22), 5663–5668 (2012).

79. Huff TB, Hansen MN, Zhao Y, Cheng JX, Wei A. Controlling the cellular uptake of gold nanorods. *Langmuir* 23(4), 1596–1599 (2007).

80. Howard MD, Jay M, Dziubla TD, Lu X. PEGylation of nanocarrier drug delivery systems: state of the art. *J. Biomed. Nanotechnol.* 4(2), 133–148 (2008).

81. Qian X, Peng XH, Ansari DO *et al. In vivo* tumor targeting and spectroscopic detection with surface-enhanced Raman nanoparticle tags. *Nat. Biotechnol.* 26(1), 83–90 (2008).

82. Yang J, Shen D, Zhou L *et al.* Spatially confined fabrication of core-shell gold nanocages@mesoporous silica for near-infrared controlled photothermal drug release. *Chem. Mater.* 25(15), 3030–3037 (2013).

83. Liz-Marzán LM, Giersig M, Mulvaney P. Synthesis of nanosized gold-silica core-shell particles. *Langmuir* 12(18), 4329–4335 (1996).

84. Song Z, Liu Y, Shi J *et al.* Hydroxyapatite/mesoporous silica coated gold nanorods with improved degradability as a multi-responsive drug delivery platform. *Mater. Sci. Eng. C* 83, 90–98 (2018).

85. Zheng XS, Hu P, Cui Y *et al.* BSA-coated nanoparticles for improved SERS-based intracellular pH sensing. *Anal. Chem.* 86(24), 12250–12257 (2014).

86. Rengan AK, Jagtap M, De A, Banerjee R, Srivastava R. Multifunctional gold coated thermo-sensitive liposomes for multimodal imaging and photo-thermal therapy of breast cancer cells. *Nanoscale* 6(2), 916–924 (2014).

87. Feng W, Nie W, Cheng Y *et al. In vitro* and *in vivo* toxicity studies of copper sulfide nanoplates for potential photothermal applications. *Nanomed. Nanotechnol. Biol. Med.* 11(4), 901–912 (2015).

88. Sun M, Sundaresan G, Jose P *et al.* Highly stable intrinsically radiolabeled indium-111 quantum dots with multidentate zwitterionic surface coating: dual modality tool for biological imaging. *J. Mater. Chem. B* 2(28), 4456–4466 (2014).

89. Shan Y, Ma S, Nie L *et al.* Size-dependent endocytosis of single gold nanoparticles. *Chem. Commun.* 47(28), 8091–8093 (2011).

90. Mou J, Liu C, Li P *et al.* A facile synthesis of versatile $Cu_{2-x}S$ nanoprobe for enhanced MRI and infrared thermal/photoacoustic multimodal imaging. *Biomaterials* 57, 12–21 (2015).

91. Hauck TS, Ghazani AA, Chan WCW. Assessing the effect of surface chemistry on gold nanorod uptake, toxicity, and gene expression in mammalian cells. *Small* 4(1), 153–159 (2008).

92. Oh N, Park JH. Surface chemistry of gold nanoparticles mediates their exocytosis in macrophages. *ACS Nano* 8(6), 6232–6241 (2014).

93. Huo S, Jin S, Ma X *et al.* Ultrasmall gold nanoparticles as carriers for nucleus-based gene therapy due to size-dependent nuclear entry. *ACS Nano* 8(6), 5852–5862 (2014).

94. De Jong WH, Hagens WI, Krystek P, Burger MC, Sips AJAM, Geertsma RE. Particle size-dependent organ distribution of gold nanoparticles after intravenous administration. *Biomaterials* 29(12), 1912–1919 (2008).

95. Rycenga M, Wang Z, Gordon E *et al.* Probing the photothermal effect of gold-based nanocages with surface-enhanced Raman scattering (SERS). *Angew. Chem. Int. Ed.* 48(52), 9924–9927 (2009).

96. Von Maltzahn G, Centrone A, Park JH *et al.* SERS-coded gold nanorods as a multifunctional platform for densely multiplexed near-infrared imaging and photothermal heating. *Adv. Mater.* 21(31), 3175–3180 (2009).

97. Kircher MF, De La Zerda A, Jokerst JV *et al.* A brain tumor molecular imaging strategy using a new triple-modality MRI-photoacoustic-Raman nanoparticle. *Nat. Med.* 18(5), 829–834 (2012).

98. Lu W, Singh AK, Khan SA, Senapati D, Yu H, Ray PC. Gold nano-popcorn-based targeted diagnosis, nanotherapy treatment, and *in situ* monitoring of photothermal therapy response of prostate cancer cells using surface-enhanced Raman spectroscopy. *J. Am. Chem. Soc.* 132(51), 18103–18114 (2010).

99. Jung S, Nam J, Hwang S, *et al.* Theragnostic pH-sensitive gold nanoparticles for the selective surface enhanced Raman scattering and photothermal cancer therapy. *Anal. Chem.* 85(16), 7674–7681 (2013).

100. Gao Y, Li Y, Chen J *et al.* Multifunctional gold nanostar-based nanocomposite: synthesis and application for noninvasive MR-SERS imaging-guided photothermal ablation. *Biomaterials* 60, 31–41 (2015).

101. Deng L, Li Q, Yang Y *et al.* 'Two-step' Raman imaging technique to guide chemo-photothermal cancer therapy. *Chem. A Eur. J.* 21(48), 17274–17281 (2015).

102. Liu Z, Ye B, Jin M *et al.* Dye-free near-infrared surface-enhanced Raman scattering nanoprobes for bioimaging and high-performance photothermal cancer therapy. *Nanoscale* 7(15), 6754–6761 (2015).

103. Chen H, Liu Z, Li S *et al.* Fabrication of graphene and AuNP core polyaniline shell nanocomposites as multifunctional theranostic platforms for SERS real-time monitoring and chemo-photothermal therapy. *Theranostics* 6(8), 1096–1104 (2016).

104. Sun C, Gao M, Zhang X. Surface-enhanced Raman scattering (SERS) imaging-guided real-time photothermal ablation of target cancer cells using polydopamine-encapsulated gold nanorods as multifunctional agents. *Anal. Bioanal. Chem.* 409(20), 4915–4926 (2017).

105. Yang G, Liu Z, Li Y *et al.* Facile synthesis of black phosphorus-Au nanocomposites for enhanced photothermal cancer therapy and surface-enhanced Raman scattering analysis. *Biomater. Sci.* 5(10), 2048–2055 (2017).

106. Chen J, Sheng Z, Li P *et al.* Indocyanine green-loaded gold nanostars for sensitive SERS imaging and subcellular monitoring of photothermal therapy. *Nanoscale* 9(33), 11888–11901 (2017).

107. Gao J, Sanchez-Purra M, Huang H *et al.* Synthesis of different-sized gold nanostars for Raman bioimaging and photothermal therapy in cancer nanotheranostics. *Sci. China Chem.* 60(9), 1219–1229 (2017).

108. Wang P, Wu Q, Wang F *et al.* Evaluating cellular uptake of gold nanoparticles in HL-7702 and HepG2 cells for plasmonic photothermal therapy. *Nanomedicine* 13(18), 2245–2259 (2018).

109. Lv Q, Min H, Duan DB *et al.* Total aqueous synthesis of Au@$Cu_{2-x}S$ core-shell nanoparticles for *in vitro* and *in vivo* SERS/PA imaging-guided photothermal cancer therapy. *Adv. Healthc. Mater.* 8(2), 1801257 (2019).

110. Wen S, Miao X, Fan GC *et al.* Aptamer-conjugated Au nanocage/SiO_2 core-shell bifunctional nanoprobes with high stability and biocompatibility for cellular SERS imaging and near-infrared photothermal therapy. *ACS Sensors* 4(2), 301–308 (2019).

111. Song C, Li F, Guo X *et al.* Gold nanostars for cancer cell-targeted SERS-imaging and NIR light-triggered plasmonic photothermal therapy (PPTT) in the first and second biological windows. *J. Mater. Chem. B* 7(12), 2001–2008 (2019).

•• **Studied the fabicated gold nanotags for surface-enhanced Raman spectroscopy imaging and photothermal therapy applications in both the NIR-I and NIR-II windows.**

112. Sujai PT, Joseph MM, Karunakaran V *et al.* Biogenic cluster-encased gold nanorods as a targeted three-in-one theranostic nanoenvelope for SERS-guided photochemotherapy against metastatic melanoma. *ACS Appl. Bio Mater.* 2(1), 588–600 (2019).

113. Zhu W, Gao MY, Zhu Q *et al.* Monodispersed plasmonic Prussian blue nanoparticles for zero-background SERS/MRI-guided phototherapy. *Nanoscale* 12(5), 3292–3301 (2020).

114. Wang J, Liang D, Jin Q, Feng J, Tang X. Bioorthogonal SERS nanotags as a precision theranostic platform for *in vivo* SERS imaging and cancer photothermal therapy. *Bioconjug. Chem.* 31(2), 182–193 (2020).

115. Das A, Arunagiri V, Tsai H-C *et al.* Investigation of dual plasmonic core-shell Ag@CuS nanoparticles for potential surface-enhanced Raman spectroscopy-guided photothermal therapy. *Nanomedicine* 16(11), 909–913 (2021).

116. Sujai PT, Shamjith S, Joseph MM, Maiti KK. Elucidating gold-MnO_2 core-shell nanoenvelope for real time SERS-guided photothermal therapy on pancreatic cancer cells. *ACS Appl. Bio Mater.* 4(6), 4962–4972 (2021).

•• **The fabricated theranostic nanoenvelope was used to demonstrate temperature-induced precise cell death mechanism through surface-enhanced Raman spectroscopy spectral analysis in pancreatic cancer cells.**

117. Wei Q, He J, Wang S *et al.* Low-dose x-ray enhanced tumor accumulation of theranostic nanoparticles for high-performance bimodal imaging-guided photothermal therapy. *J. Nanobiotechnology* 19(1), 1–17 (2021).

118. Wei Q, Arami H, Santos HA *et al.* Intraoperative assessment and photothermal ablation of the tumor margins using gold nanoparticles. *Adv. Sci.* 8(5), 2002788 (2021).

•• **Intraoperative detection and adjuvant photothermal ablation of tumor margins were investigated using ovarian tumor model. To prove clinical translatability of this technique, the biodistribution, pharmacokinetics, Raman contrast and toxicity of these gold nanoparticles were extensively investigated.**

119. Zhang M, Xiao X, Liu L *et al.* Aptamer-conjugated biocompatible nanospheres for fluorescent imaging-guided hepatocellular carcinoma-targeted phototherapeutic modality. *Adv. Nano Biomed Res.* 2(9), 2200014 (2022).

120. He J, Hua S, Zhang D, Wang K, Chen X, Zhou M. SERS/NIR-II optical nanoprobes for multidimensional tumor imaging from living subjects, pathology, and single cells and guided NIR-II photothermal therapy. *Adv. Funct. Mater.* 32(46), 2208028 (2022).

121. Liu K, Liu K, Liu J *et al.* Copper chalcogenide materials as photothermal agents for cancer treatment. *Nanoscale* 12(5), 2902–2913 (2020).

• **Briefly demonstrates the copper-based chalcogenide nanostructures for cancer theranostics.**

122. Li Y, Lu W, Huang Q, Li C, Chen W. Copper sulfide nanoparticles for photothermal ablation of tumor cells. *Nanomedicine* 5(8), 1161–1171 (2010).

123. Yoshimi R, Tsukazaki A, Kikutake K *et al.* Dirac electron states formed at the heterointerface between a topological insulator and a conventional semiconductor. *Nat. Mater.* 13(3), 253–257 (2014).

124. Mellnik AR, Lee JS, Richardella A *et al.* Spin-transfer torque generated by a topological insulator. *Nature* 511(7510), 449–451 (2014).

125. Mohammadniaei M, Lee T, Bharate BG *et al.* Bifunctional Au@Bi_2Se_3 core-shell nanoparticle for synergetic therapy by SERS-traceable antagomiR delivery and photothermal treatment. *Small* 14(38), 1–13 (2018).

126. Wen J, Yang K, Sun S. MnO_2-based nanosystems for cancer therapy. *Chem. Commun.* 56(52), 7065–7079 (2020).

127. Yang Y, Wang C, Tian C, Guo H, Shen Y, Zhu M. Fe_3O_4@MnO_2@PPy nanocomposites overcome hypoxia: magnetic-targeting-assisted controlled chemotherapy and enhanced photodynamic/photothermal therapy. *J. Mater. Chem. B* 6(42), 6848–6857 (2018).

128. Wang L, Guan S, Weng Y *et al.* Highly efficient vacancy-driven photothermal therapy mediated by ultrathin MnO_2 nanosheets. *ACS Appl. Mater. Interfaces* 11(6), 6267–6275 (2019).

129. Barot S, Abo-Ali EM, Zhou DL, Palaguachi C, Dukhande VV. Inhibition of glycogen catabolism induces intrinsic apoptosis and augments multikinase inhibitors in hepatocellular carcinoma cells. *Exp. Cell Res.* 381(2), 288–300 (2019).

130. Petrecca K, Guiot MC, Panet-Raymond V, Souhami L. Failure pattern following complete resection plus radiotherapy and temozolomide is at the resection margin in patients with glioblastoma. *J. Neurooncol.* 111(1), 19–23 (2013).

131. Jiang C, Wang Y, Song W, Lu L. Delineating the tumor margin with intraoperative surface-enhanced Raman spectroscopy. *Anal. Bioanal. Chem.* 411(18), 3993–4006 (2019).

•• **Briefly discusses the use of nanotags in intraoperative surface-enhanced Raman spectroscopy image-guided resection and presents their potential in detection of the actual tumor lesion with high specificity and sensitivity.**

132. Karabeber H, Huang R, Iacono P *et al.* Guiding brain tumor resection using surface-enhanced Raman scattering nanoparticles and a hand-held Raman scanner. *ACS Nano* 8(10), 9755–9766 (2014).

133. Harmsen S, Huang R, Wall MA *et al.* Surface-enhanced resonance Raman scattering nanostars for high-precision cancer imaging. *Sci. Transl. Med.* 7(271), 271ra7 (2015).

134. Das A, Arunagiri V, Tsai HC, Prasannan A, Moirangthem RS. Core-multishell Au@$Cu_{2-x}S$@ Au nanoparticles for surface-enhanced Raman scattering-guided low-intensity photothermal cancer therapy. *ACS Appl. Nano Mater.* 4(11), 12278–12288 (2021).